STOICHIOMETRY DEPENDENCE OF THE EVOLUTION OF THE IRRADIATED-INDUCED DEFECT CLUSTERS IN LANTHANUM-DOPED CERIA

BY

WEI-YING CHEN

THESIS

Submitted in partial fulfillment of the requirements
for the degree of Master of Science in Nuclear Engineering
in the Graduate College of the
University of Illinois at Urbana-Champaign, 2011

Urbana, Illinois

Master's Committee:

Professor James F. Stubbins, Chair
Professor Brent J. Heuser

ABSTRACT

To study the stoichiometry dependence of irradiation effects in fluorite-type mixed oxide nuclear fuel ($UPuO_2$), ion implantation in La doped ceria (with chemical formula as $Ce_xLa_{1-x}O_{1.5+0.5x}$) was used.Cerium dioxide single crystals with 0 mol%, 5 mol% and 25 mol% La concentration were irradiated with 1 MeV Kr ions at 800°C. In-situ transmission electron microscope (TEM) was utilized to observe the the damage process and defects created by the ion beam irradiation. Dislocations loops were observed after irradiation and were determined to be on {111} planes, but not on {220} or {200} planes. A substantial difference in the average size of dislocation loops for 0 %, 5% and 25% cases was observed at several doses.The growth rate of dislocation loops and the oxygen vacancy diffusivity were found to be inversely correlated.

To my parents, for their love and support.

ACKNOWLEDGMENTS

This project would not have been possible without the support of many people. Firstly, I would like to express my gratitude to my advisor Prof. James F. Stubbins for his guidance and support toward my professional development.

I would like to thank researchers in Argonne National Laboratory, Dr. Mark A. Kirk, Peter Baldo and Edward Ryan. Without them, it was not possible for me to explore any exciting scientific observations in this research. Special thanks to Dr. Kirk for his valuable advise in TEM operation and interpretation.

I would like to thank staffs in Material Research Laboratory in UIUC, especially Jianguo Wen, Changhui Lei, Wacek Swiech, Mauro Sardela and Doug Jeffers. Without their training and help, my work could never have been finished.

I would like to thank my colleagues, Bei Ye, Di Yun, Aaron Oaks, Yinbin Miao and Brian Kleinfledt. Special thanks to Bei for teaching me how to operate a TEM and to conduct irradiation experiments. Many thanks to Aaron for his patient review on my thesis.

Finally, I greatly appreciate the support from my family and I would like to dedicate this thesis to them.

TABLE OF CONTENTS

CHAPTER 1

INTRODUCTION

Power upgrade of current Generation II nuclear power plants is intensely demanded because of increasing electricity demand and petroleum price. One of the method to realize power upgrade is to reduce the safety margin originating from the uncertainty in calculations. For many years most of the focus in this area has been on neutronics and thermal hydraulics calculations.Accuracy improvement in material properties has been comparatively slower due to their complicated nature, especially under irradiation.

Irradiation (e.g., fission products and γ rays) creates point defects in the relatively perfect crystals in the fuel, cladding, pressure vessel or other structural materials. As time goes by, these point defects migrate, annihilate and cluster, and could gradually change the macroscopic properties of the materials, resulting in swelling, embrittlement and corrosion [1][2]. The change in macroscopic properties is an overall result from a change in microscopic structures. Thus in order to achieve better predictions on the material degradation under irradiation, a microscopic understanding on the irradiation-material interactions is required.

Uranium dioxide(UO_2), which forms in the fluorite crystal structure, is considered as a stable and radiation resistant material and is the dominant fuel type in modern nuclear reactors.Cerium oxide (CeO_2) shares many similar material properties with UO_2, including crystal structure, thermal conductivity, and high melting point [3], and is used in this study as a surrogate for UO_2 [4][5][6][7][8][9].

With more advanced microscopy techniques and computer calculation capabilities,it is now possible to understand more detailed micro-structural change and thus make better predictions. Experiments and computer calculations are both important and complementary, since experimental results provide benchmarks for computer simulations, and in return, computer simulation help explain details that are beyond the resolving power of experi-

ments.

Several experimental and computing simulations have been done on radiation effects in CeO_2. With high-energy electron irradiation (200∼3000 KeV), interstitial type dislocation loops were found on $(\frac{1}{9})\{111\}$ or $(\frac{1}{2})\{110\}$ planes depending on whether the Ce interstitials are part of the loop structure or not [4][5]. Yasunaga et al. proposed that $(\frac{1}{9})\{111\}$ dislocation loops are entirely composed of oxygen interstitials when the energy of incident electrons is too low to displace cerium ions [4]. While electron energy is greater than 1500 keV, cerium ions start to be displaced from lattice site and $(\frac{1}{2})\{110\}$ dislocation loops begin to appear [5]. Shiiyama et al. validated the clustering of oxygen interstitials on {111} planes with molecular dynamic (MD) calculations[10]. However, doubts have arisen that this kind of configuration has a high coulomb energy and should not be stable. This controversy is one of the focuses in this study.

With swift ion irradiation (100∼200 MeV), ion tracks were formed as straight lines where electronic structures were changed along the path [6] [7]. This kind of radiation results in mostly electronic excitation and ionization and few atom displacements. Ion irradiation with energy of several MeV, however, has different effects from the former by inducing large amount of ballistic scattering and cascade. The vacancies and interstitials produced by cascade would annihilate or cluster to form dislocation loops or voids.Ye et al. observed the temperature dependence of the evolution of dislocation loops in CeO_2 with 1 MeV Krypton (Kr) [11]. It was observed that dislocation loops grew faster when temperature was higher during irradiation. After a sufficient amount of irradiation, dislocation loops began to tangle together and formed a dislocation network.

Except for stoichiometric CeO_2, hyper-stoichiometric CeO_2 doped with trivalent ions was also studied in order to simulate UO_2 fuel containing fission products.Results from this study would be useful for normal nuclear fuel after some operating period or the fuel used in reprocessing reactors. Elements have been doped into CeO_2 in order to study the impurity effect during irradiation. CeO_2 doped with erbium (Er) and gadolinium (Gd) irradiated with 200 MeV xenon (Xe) ions showed that Er and Gd ions had increased the lattice parameter expanding rate under irradiation [8][9]. Beside lattice parameter, microstructure changes in La-doped CeO_2 under irradiation were studied by Yun et al. who found that higher concentrations of Lanthanum

(La) in CeO_2 caused slower defect kinetics at 600 °C [12]. The dependence of defect clusters evolution on impurity concentration is another main concern in this study.

Apart from experiments, several computer simulations have been done to explore the nature and kinetics of defect clustering. Aidhy et al. found the oxygen interstitials would cluster more aggressively when oxygen vacancies were trapped by cation ions [13]. Jonnet numerically calculated a set of governing equations based on rate theory to simulate the size and density of dislocation loops during irradiation [14].

In this study, energetic ion irradiation with 1 MeV Kr in $Ce_xLa_{1-x}O_2$ (x = 0.95, 0.75) was carried out at 800°C ,while in-situ TEM was implemented to record the evolution of defect clusters. Characterization and measurement were done on the dislocation loops and compared to previous studies [11][12] to explain the La effect on CeO_2 under irradiation.

CHAPTER 2

GOAL AND APPROACH

The objective of this study is to determine the effect of La on the evolution of dislocation loops under energetic ion irradiation at high temperature in order to simulate the material degradation of UO_2 in a nuclear reactor.

In order to accomplish this, a combination of accelerator and electron microscope was used to simulate what happens in nuclear reactor fuel. $CeO_2$was used as a surrogate in this study to simulate UO_2. La was used as a dopant to simulate trivalent fission products. High energy ions from a particle accelerator was used to cause ion displacements in CeO_2 in order to simulate the radiation damage. The energy level of the accelerated ions was chosen to be high enough to mostly penetrate the CeO_2 film without being implanted but, at the same time, low enough to produce enough displacements in the film instead of just electronic excitation and ionization. Figure 2.1 (a) shows the SRIM calculation for 1 MeV Kr ions bombarding 160 nm 5 mol% La doped CeO_2 on strontium titanate ($SrTiO_3$) substrate, which illustrates that most of the Kr ions would not be stopped inside the film [15]. Besides, the vacancy distribution showed in Figure 2.1 (b) is reasonably flat in CeO_2 layer, which means the point defects would be generated relatively uniformly.

Dislocation loops are the centeral interest of this study because they are the direct result of point defect kinetics. The growth rate of dislocation loops can be obtained by monitoring a single loop continuously or by averaging all of the loop sizes in an area at different doses (the latter was used in this research). To maintain consistency and accuracy, both the area where images were taken and the diffraction condition were held as close to constant as possible.

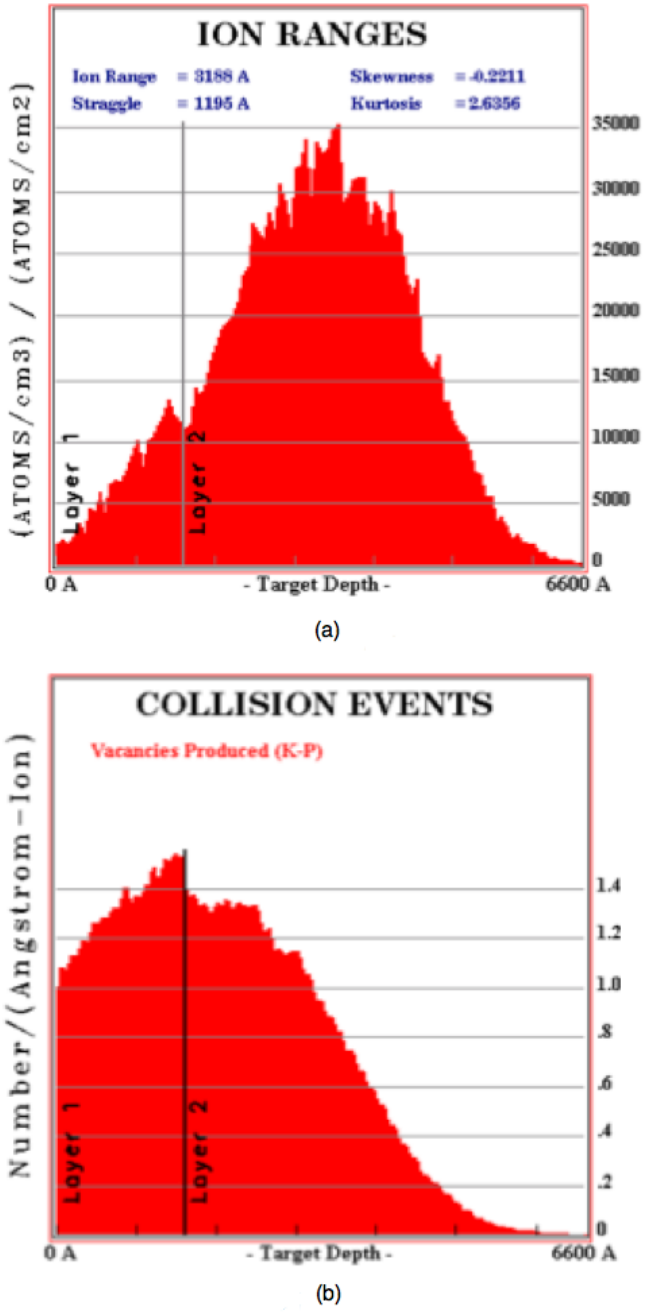

Figure 2.1: SRIM calculation (a)1MeV Kr ion range and (b) vacancy range. Layer 1: 160 nm $Ce_{0.95}La_{0.05}O_{1.975}$. Layer 2: $SrTiO_3$

CHAPTER 3

BACKGROUND

3.1 Material Properties of CeO_2 and La doped CeO_2

In the past, CeO_2 and doped CeO_2 were mostly studied for their applications in catalysist and oxygen sensor in automobile exhaust/emission system [16]. Because of its high electrical and thermal conductivity, it is one of the candidates for fuel cell electrode [16]. The knowledge of material properties and defect chemistry of ceria and doped ceria have been provided through these studies.

Cerium(IV) dioxyde (CeO_2) has a fluorite crystal structure with a lattice constant 5.41134 Å. Fluorite structure is a fcc lattice with a basis composed of one Ce and two oxygen. As shown in Figure 3.1, Ce ions (Ce^{4+}) reside at the corners and the face-centers of a conventional unit cell while oxygen ions (O^{2-}) reside in the tetrahedral interstitial sites, $[\frac{1}{4}\ \frac{1}{4}\ \frac{1}{4}]$.

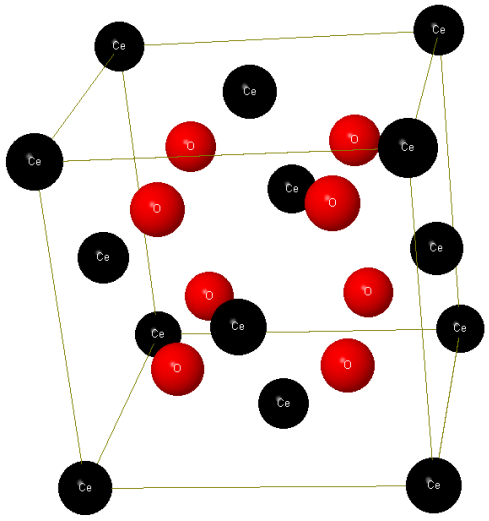

Figure 3.1: The crystal structure of CeO_2

CeO_2 has many properties similar to UO_2 so it is a popular surrogate to UO_2. First above all, CeO_2 and UO_2 both have the same fluorite structure. In addition, their melting temperature are similar. The melting temperature for CeO_2 is 2600 °C and that for UO_2 is 2870 °C. Their thermal conductivity is similar as well. Up to 700 °C, all these properties have been characterized [3][4][6][17].

When CeO_2 is doped with trivalent ions like yttrium(III) and lanthanum(III), these trivalent ions will occupy Ce sites as substitutional impurities, provided that the concentration of trivalent ions is below the solubility. The dependence of electrical conductivity on the trivalent concentration is controlled by two mechanisms.

Firstly, when a trivalent ions is doped into cerium oxide by substituting a cerium ion, a local charge imbalance is created. On thermal equilibrium state, this charge imbalance must be compensated in three ways which are oxygen vacancy compensation, dopant interstitial compensation and cerium interstitial compensation [18].

The oxygen vacancy compensation is energetically favored over the others. An oxygen vacancy is created for every two La ions which replace two host Ce ions in the cation lattice. In dopant interstitial compensation, three Ce host ions must be replaced by dopant ions when a dopant is placed in an interstitial site. Finally, cerium interstitial compensation need one Ce ions to be placed in an interstitial site every four dopant ions placed in the host Ce sites. The latter two have higher defect energy thus rarely exist[18].

Because of the oxygen vacancy compensation, doped ceria has higher oxygen vacancy concentration with higher dopant concentration. Since electrical conductivity is positively dependent on the oxygen vacancy diffusivity, the higher concentration of oxygen vacancies cause higher oxygen vacancy diffusivity, and thus electrical conductivity.

Secondly, Minernivi et al. calculated the binding energy of a series of trivalent ions with oxygen vacancies in CeO_2 [18]. The results showed that the trivalent ions always have a positive binding energy with oxygen vacancies, which indicates that dopant ions would trap oxygen vacancies. As a result, this mechanism will decrease the oxygen vacancy diffusivity with increasing dopant ion concentration.

The two mechanisms described above compete each other and result in a maximum oxygen vacancies diffusivity around a dopant concentration of 3

mol% to 5 mol% [19][20]. Figure 3.2 is an example for yittrium doped CeO_2 [21].

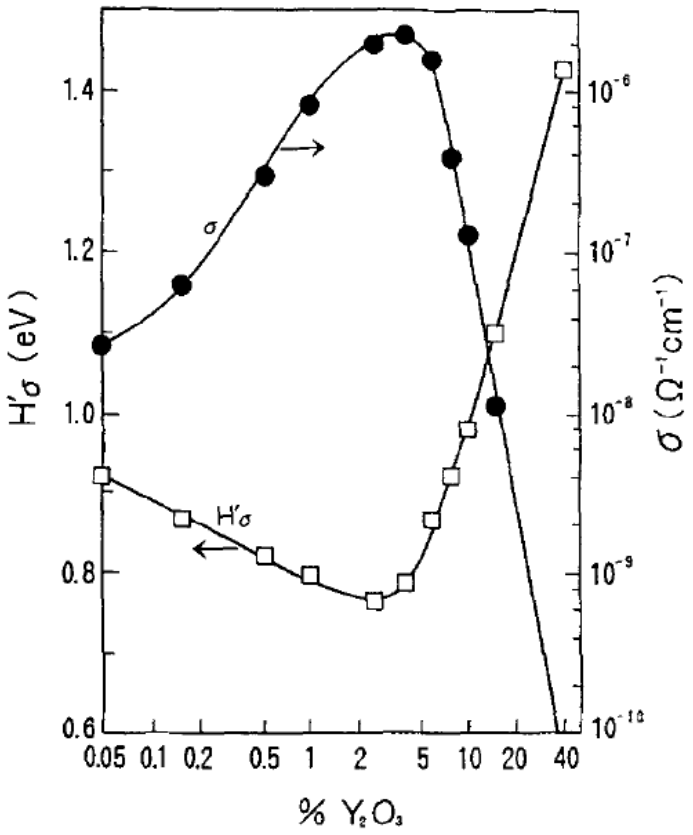

Figure 3.2: Low temperature activation enthalpy, H'$_\sigma$ and electrical conductivity σ at 182C of yttria-doped ceria as a function of dopant concentration [21]

3.2 Diffraction Contrast in a Transmission Electron Microscope

The appearance of TEM images greatly depends on the diffraction condition being used. In order to obtain the highest contrast, reflections from only one diffracted spot (one single set of planes) was used to form images. The idea is similar to taking pictures of a person's wrinkles: it would only appear clearly when the light was projected from single direction. If the light was projected from all directions, the shadow of wrinkles would be averaged out

and become invisible.

When the incident beam is used, the images formed are called bright field images. Otherwise, when the deflected beam is used, the images formed are called dark field images. Dark field images in general give better contrast. In addition to choosing only one diffraction spot to form images, TEM sample is also tilted in such that only one set of planes is excited. In terms of a diffraction pattern, this means that only a certain system of planes is made bright but others darkened. (This is a general technique. Readers are referred to any TEM textbook for more detail.) The diffraction condition g = (220) (strongly excited) was used to take sequential images through the entire irradiation process since this condition was considered to give best image[22].

In addition to using the dark field condition, the electron beam can be further weakened by tilting the sample relative to the electron beam so in the diffraction pattern the incident spot is moved away from the Kikuchi band (mostly 220 band for this study). By dong this, the diffraction from the specific planes is reduced, resulting in increased resolution on defect contrast. For instance, Fig 3.3(a) and Fig 3.3(b) demonstrate the difference between strong diffraction condition and weak diffraction condition. It is obvious that the weak-beam dark field image gives the better resolution.

Using Kikuchi patterns to identify the orientation of the sample is an important technique in this study. The reason we form Kikuchi patterns is described below. When the specimen is thick enough, most incident electrons will be scattered several times. In this case, a significant amounts of electrons travel in all direction are generated inside a specimen. These electrons travelling in all direction are called diffuse electrons. Since the energy loss for each scattering event is small compared to the incident energy, we can assume diffuse electrons hold the same wavelength λ as incident electrons.

Since the diffuse electrons travel in all directions, the wave vectors k satisfying the Bragg condition for certain plane hkl is now of a range, compared to normal diffraction patterns where only a single k-vector satisfies the Bragg condition. As is shown in Figure 3.4, collecting this range of k-vectors forms two cones called Kossel cones. The cones intercept the Ewald sphere to form parabolas. In diffraction patterns, the parabolas are approximately parallel lines which are the eventual Kikuchi lines being observed.

The cones in Figure 3.4 are fixed to the plane hkl. So when we tilt the

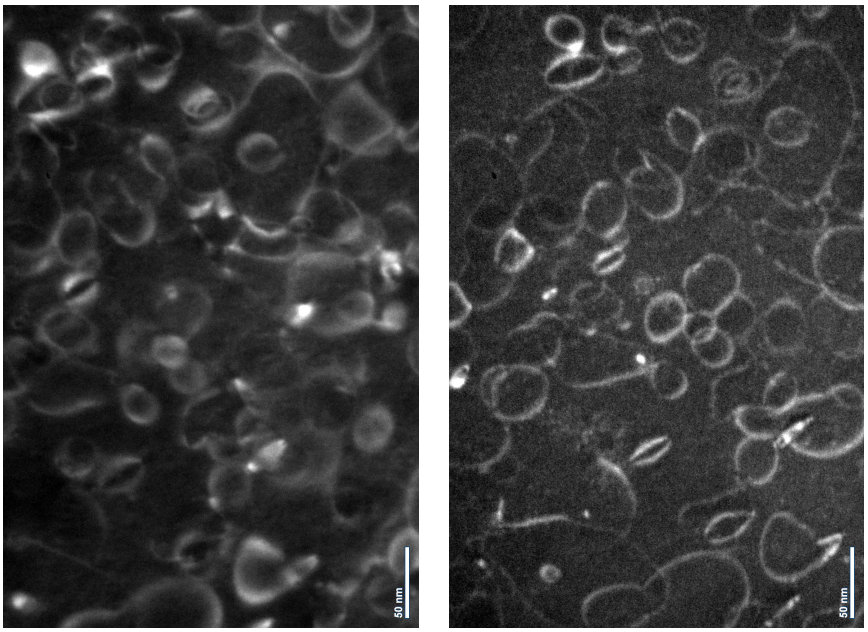

(a) Stronger (b) Weaker

Figure 3.3: CeO_2 with 25 % La at a dose of 8×10^{14} ions/cm2 with (a) stronger and (b) weaker diffraction conditon

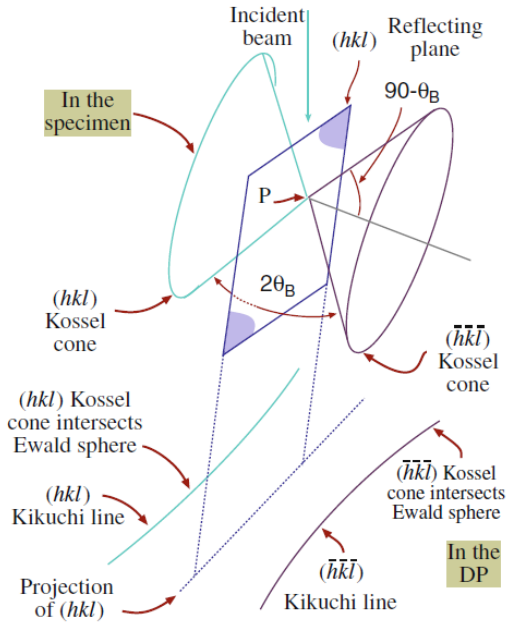

Figure 3.4: The formation of Kikuchi pairs in a Kikuchi pattern [23]

crystals, the Kikuchi lines also move. The diffraction patterns do not change their positions when the crystals are tilted. The intensity of the spots in the diffraction patterns do change with orientation but not sensitive. This is the reason Kikuchi pattern are used to identify the relative orientation of the specimens with incident beams.

3.3 Molecular Statics and Dynamics

Molecular statics and dynamics are computer simulation techniques to simulate material properties on atomistic scales. In molecular statics, the atomic systems are relaxed at 0 K to minimize the energy locally. Since the temperature is at absolute zero, no kinetic energy is concerned. The total energy is given entirely by the potential energy of the system. The potentail between atoms is complex and is mostly simplified to spherical and two atom interaction. Such simplification is performed because, firstly, it is hard to derive complex potentials. Secondly, it is time-consuming to consider these higher-order interactions.

The Buckingham form is one of the most popular pair potential forms used nowadays. It consists of a repulsion and an attraction terms. Plus the Coulomb term, the formula for pair potential is described in the equation below.

$$U_{ij} = \frac{q_i q_j e^2}{4\pi\epsilon_0 r} + A_{ij} exp^{-\frac{r}{\rho_{ij}}} - \frac{C_{ij}}{r^6}$$

U_{ij} is the pair potential between ion i and j. The distance is r between ion i and j. Parameters A_{ij}, ρ_{ij} and C_{ij} are obtained by fitting to materials properties like lattice constants and elastic constants. When polarization effects are considered, a core-shell model, proposed by Dick and Overhauser [24], is implemented by treat ions as massless electron cloud (negatively charged shell) and a massive nucleus (positively charged core) connected by a massless spring. The spring constants could be determined by fitting the polarization properties of the materials.

Among many potentials developed for $Ce_xLa_{1-x}O_{1.5+0.5x}$, Gotte potential was considered as best to describe oxygen self-diffusivity as a function of La concentrations [25][26]. The value of parameters were listed in Table 3.1.

Table 3.1: Parameters of Gotte Pair Potential

Parameters	Units	Values
O shell charge	e	-6.5667
O core charge	e	4.5667
O spring constant	eV/Å^2	1759.8
Ce shell charge	e	4.6475
Ce core charge	e	-0.6475
Ce spring constant	eV/Å^2	43.451
O - O interactions		
A	eV	9533.421
ρ	Å	0.234
C	Å^6	224.88
O - Ce interactions		
A	eV	755.1311
ρ	Å	0.429
C	Å^6	0

In Molecular Dynamics (MD), the same potential between atoms is used as in molecular statics. However, atoms have kinetic energies as well as potential energies now.The time and spatial evolutions are captured by using Verlet formulas as showed below. The future positions and velocities of an atom or ion are determined by the current positions, velocities and accelerations.

$$\overrightarrow{r}(t+\triangle t) = \overrightarrow{r}(t) + \overrightarrow{v}(t) \triangle t + \frac{\overrightarrow{a}(t) \triangle t^2}{2} + O(\triangle t^3)$$

$$\overrightarrow{v}(t+\triangle t) = \frac{\overrightarrow{x}(t+\triangle t) - \overrightarrow{x}(t-\triangle t)}{2 \triangle t} + O(\triangle t^2)$$

The acceleration of an atom at time t is equal to the summation of acceleration caused from all the other atoms in the system. The acceleration is equal to the force divided by mass, $\overrightarrow{a}(t) = \frac{\overrightarrow{F}(t)}{m}$. The force on atom i exerted by atom j is equal to the minus gradient of the pair potential between atom i and j, $\overrightarrow{F}(t) = - \bigtriangledown U_{ij}(\overrightarrow{r}(t))$ where $\overrightarrow{r}(t)$ is the position of atom i.

The time scale limit for MD simulation is on the order of picoseconds, thus it is difficult to simulate long-term process like diffusion or defect cluster evolution which occur on a time scale of microseconds and longer. In addition, because of its time scale limitation it is hard to compare MD simulations with experimental results : the duration of the experiments is from minutes to hour). This is especially true when the interest is on the diffu-

sion of heavy ions (Ce, for example, in this study) which have a relatively low diffusion coefficient. This problem could be solved by another atomistic simulation technique, Kinetic Monte Carlo (KMC), which will be introduced in the next section.

3.4 Kinetic Monte Carlo Simulations

Suppose a system has some process that can occur with reaction rate r_i. In this research, the processes are the jumps of ions (oxygen) into nearby sites. The algorithm of KMC is as followed:

1. Initialize the system at t = 0.
2. Form a list of possible events with reaction rate r_i.
3. Calculate the cumulative rate R_i for events i by setting $R_i = \sum_{j=1}^{i} r_i$ where i is from 1 to N. Let R_N to be the total rate sum.
4. Randomly choose a number $\rho 1$ between 0 and 1.
5. Find i satisfying $R_{i-1} < R\rho < R_i$.
6. Carry out event i.
7. Update the event list and corresponding reaction rate r_i. Updating the event list is necessary because the action being carried out could change the possible events.
8. Randomly choose a number $\rho 2$ between 0 and 1.
9. Update the simulation time t = t + -ln($\rho 2$)/R.
10. Loop back to step 2 and repeat until desired simulation time has been achieved.

The reaction rate, r_i, is defined as

$$r_i = \nu_0 e^{-\frac{\triangle E_m^i}{k_B T}}$$

$\triangle E_m^i$ is the energy barrier for thermally activated process i. For this research, it is the oxygen migration energy. ν_0 is the atom (oxygen in this

research) jump frequency that describe how fast an atom attempt to migrate. T is the absolute temperature of the system. k_B is the Boltzmann constant.

CHAPTER 4

SPECIMENS AND INSTRUMENTS

4.1 Specimen Preparation

This study used plan-view TEM specimens. The detailed sample preparation process is described as follows.

First, bulk specimens were prepared as CeO_2 single crystal thin films on $SrTiO_3$ substrates by molecular beam epitaxy (MBE). Each film had one of its (100) planes parallel to the surface of substrate, which was confirmed by XRD examination (chapter 5.1). The dimension of each specimen was 14 mm × 14 mm × 1mm. La was doped into the thin film during deposition with stoichiometry being 0%(undoped), 5% and 25%. After the growth stage finished, the temperature was reduced to 200°C-300°C in 5-10 minutes and was held for 5 minutes or so before cooling down to room temperature. Ozone was still on during the cooling stage. Specifications are listed in Table 4.1.

Bulk specimens were then annealed at 1150°C for 20 hours or more in an excessive oxygen environment. This is to reduce the unfavored film structure (Figure 4.1 and Figure 4.2). The excessive oxygen environment is to prevent loss of oxygen in CeO_2 film under high temperature. The unfavored structure might come from columnized structure developed during MBE deposition, or from an uneven sputtering rate when ion milled due to a nonuniform distribution of La in film. This unfavored structure is more obvious in doped specimens, but not so much in undopd specimens.

Table 4.1: MBE Thin Film Growing Conditions

Growth Temperature	700 ± 15 C
Growth Rate	0.1 Å/ sec
Final Film Thickness	1500 - 2000 Å
Ozone Partial Pressure	∼ 100 %

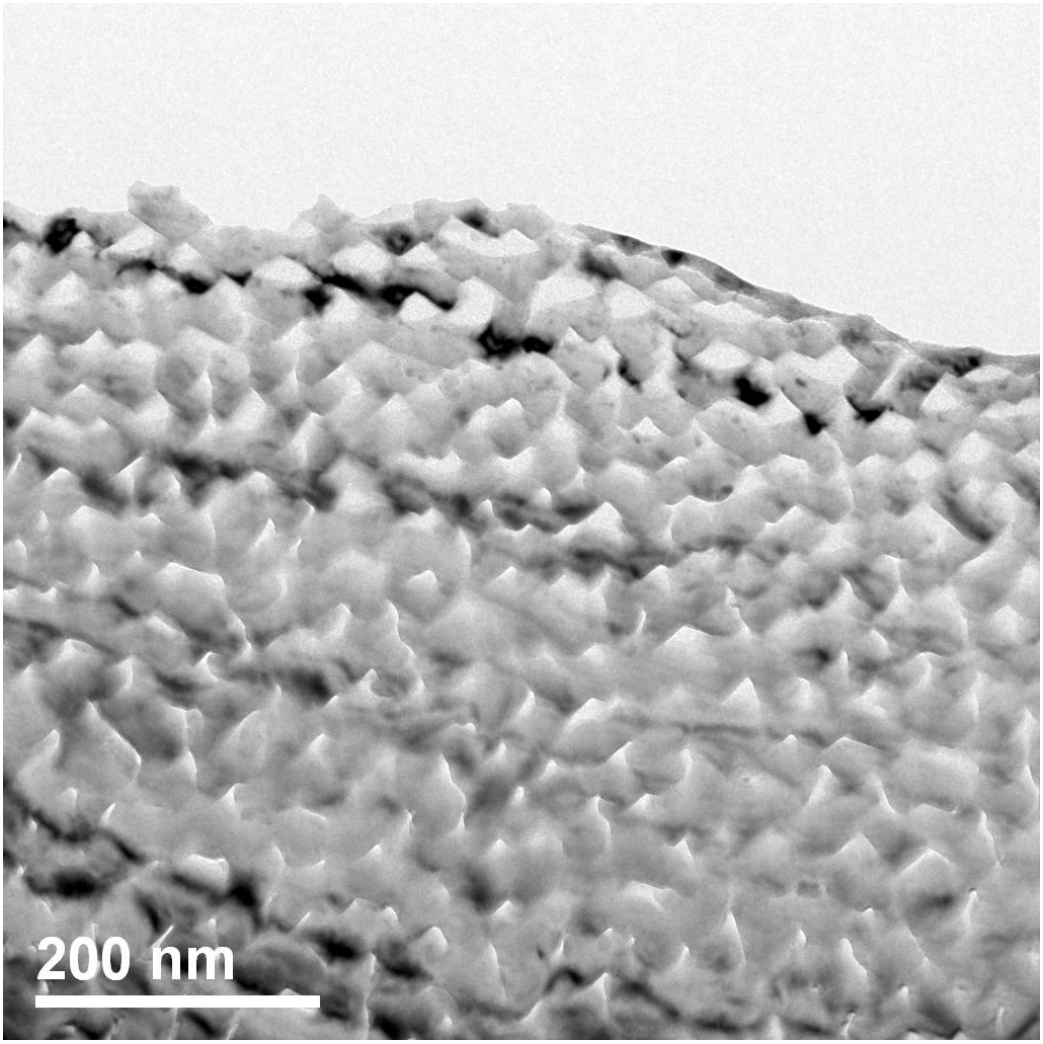

Figure 4.1: As-prepared 5% La doped TEM specimens without annealing in advance

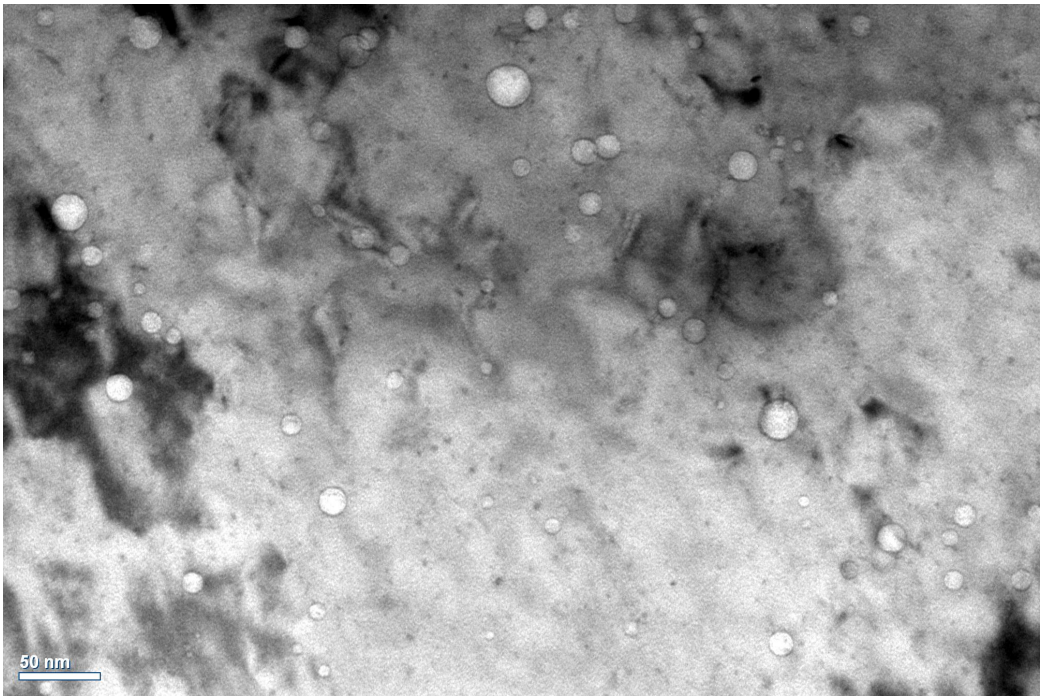

Figure 4.2: As-prepared 5% La doped TEM specimens with annealing after growth. The bubbles here are from film growth. The nature of these large bubbles are not clear but they do no seem to interact with defect clusters during *in situ* experiments

After annealing, the specimens were examined by X-ray analysis in order to confirm the crystallography. Then the bulk specimens were cut into small bars with a Buehler diamond saw. The bars have a film area of 1.5 mm $\times$ 7 mm. The specimen was then mounted on a tripod with Crystalbond so CeO_2 film faced the stage and the substrate would be mechanically removed first. using carbon nitride powder and diamond flapping film, the specimens were mechanically thinned down to around 30 μm and then cut into smaller square pieces. Each piece of specimen was then glued to a grid. The most common grid used in TEM is made of copper, however molybdenum grids were used in this study because of the high temperature (800°C) environment of the experiments.

The specimens were than ion milled with 5 keV Ar ions from substrate side until a hole in the center appeared. Once the hole appeared, the energy of Ar ions were reduced to 3 keV to polish for 15 minutes. When finished, there was a thin region around the edge of the hole that was thinner than 1000 Å, which is in general the maximum thickness that electrons can penetrate a specimen in TEM. The incident angle of Ar ions used was about 6° (which is smaller than typical value of 15°) in order to have a larger area of thin region.

4.2 Instruments and Facility

A Transmission Electron Microscope (TEM) is a microscope using electron beams to interact with very thin specimens (several hundreds of nano-meters in general). Transmitted electrons are collected with a fluorescent screen or a camera. Magnifying images and getting diffraction patterns are the two most basic operations.

As mentioned in chapter 3.4, this study contains *ex situ* and *in situ* TEM experiments. For *ex situ* experiments, bulk specimens were irradiated in the beginning and made into TEM specimens afterward. The accelerator used to produce high energy ions was Van de Graaff accelerator located at Materials Research Lab (MRL) at the University of Illinois at Urbana-Champaign (UIUC). This accelerator operate at energies up to 2.3 MeV for H, He, Ar, Kr , Xe and Ne with 1-2-3-4.5 mm beam-size apertures. Since the accelerator is old, it's difficult to maintain a stable current when the ion

energy is lower than 700 keV. This means it is not very suitable for bubble formation observation. A heating stage which is capable of temperature up to 1200°C can be used in this system, which made our high temperature experiments possible.

There are several TEMs available in MRL. Most of the work were done on a JEOL 2010 Lab6. One of the advantage of this model is the wide tilt-angle available from its double-tilt holder. This feature is important because this study need to tilt the specimen relative to the electron beam in order to get the best diffraction condition.

For *in situ* experiments, bulk specimens were firstly made into TEM specimens and then irradiated. These experiments were conducted in IVEM-TANDEM facility at Argonne National Lab. IVEM-TANDEM is a TEM interfaced with two accelerators for *in situ* ion beam studies on ion implantation and irradiation damage. The two accelerators are, respectively, 650 kV NEC ion implanter and 2 MV NEC Tandem Accelerator ,both of whose technical specifications are listed in Table 4.2. Besides a wide variety of ion sources, there are many holders as well as heating stages available for different purposes. Unlike Van de Graaff accelerator at UIUC, the IVEM provides a stable current for low energy ions therefore suitable to implant noble gases to form bubbles. A combination of ion beam irradiation and *in situ* TEM observations makes IVEM-TANDEM a one-of-a-kind facility to study defect evolution in nuclear fuel. However, one drawback of its is that the flux is smaller then other dedicated accelerators, so it is not very suitable for very high dose experiment.

Philips X'pert X-ray diffractometer(XRD) in MRL is used to characterize the crystallography of the CeO_2 thin film, specifically crystal orientation and lattice constant. A θ - 2θ scan was done to confirm that the thin film is

Table 4.2: Irradiation Instrument And Selected Specifica

Species and Operating Voltage (MV)	Accelerotor	Typical Ion Species	Typical flux ($cm^{-2}s^{-1}$)
Low Energy Positive Ions 0.02-0.6	650 kV NEC Ion Implanter	Noble Gases, H, Fe, Ni, Cu, Au	1×10^{12}
High Energy Positive Ions 0.3-5.0	2 MV NEC Tandem Accelerator	Noble Gases, H, S, Fe, Ni, Cu, Au	1×10^{12}

was a single crystal with its [100] direction perpendicular to the substrate. In addition, the lattice constant can be measured for samples of different concentration of lanthanum. By comparing to reported values, the real concentration of lanthanum can be deduced for each specimen.

CHAPTER 5

RESULTS AND DISCUSSION

5.1 X-ray Characterization of Samples Before Irradiation

The as-grown samples were investigated by Philips X'pert XRD before being made into TEM samples. The results for two kinds of samples (5 mol% La doped CeO_2 and 25 mol%La CeO_2) are shown in Figure 5.1. XRD results show that both samples are single crystal with [100] direction vertical to specimen surface. The (200) peak of the two samples occur at different θ, indicating that the lattice parameters of two samples are different because of different La concentrations. The lattice parameter is 5.417 $\mathring{A}$ for 5 mol% La sample and 5.476 Åfor 25 mol % La one. Compared to previous study on lattice parameter dependence on impurity concentration in CeO_2 [27] as is shown in Figure 5.2, the actual La concentration is around 3.3 mol% for 5 mol% La sample and 22 mol% for 25 mol% La sample. However, 5 mol% and 25 mol% are still used to name the samples for convenience.

5.2 Defect Cluster Evolution Under Irradiation

The observation on the evolution of dislocation loops during irradiation is presented below. Figure 5.3 - 5.10 shows the defect structure in the 5 mol% La doped sample at various doses levels. All images were taken at the same area and the same diffraction condition except for that last two doses due to the significant bending of the film.

Those micrographs show the evolution of dislocation loops under energetic ion irradiation at elevated temperature: nucleation and growth of dislocation loops, interaction of loops to form larger loops, and the transformation of

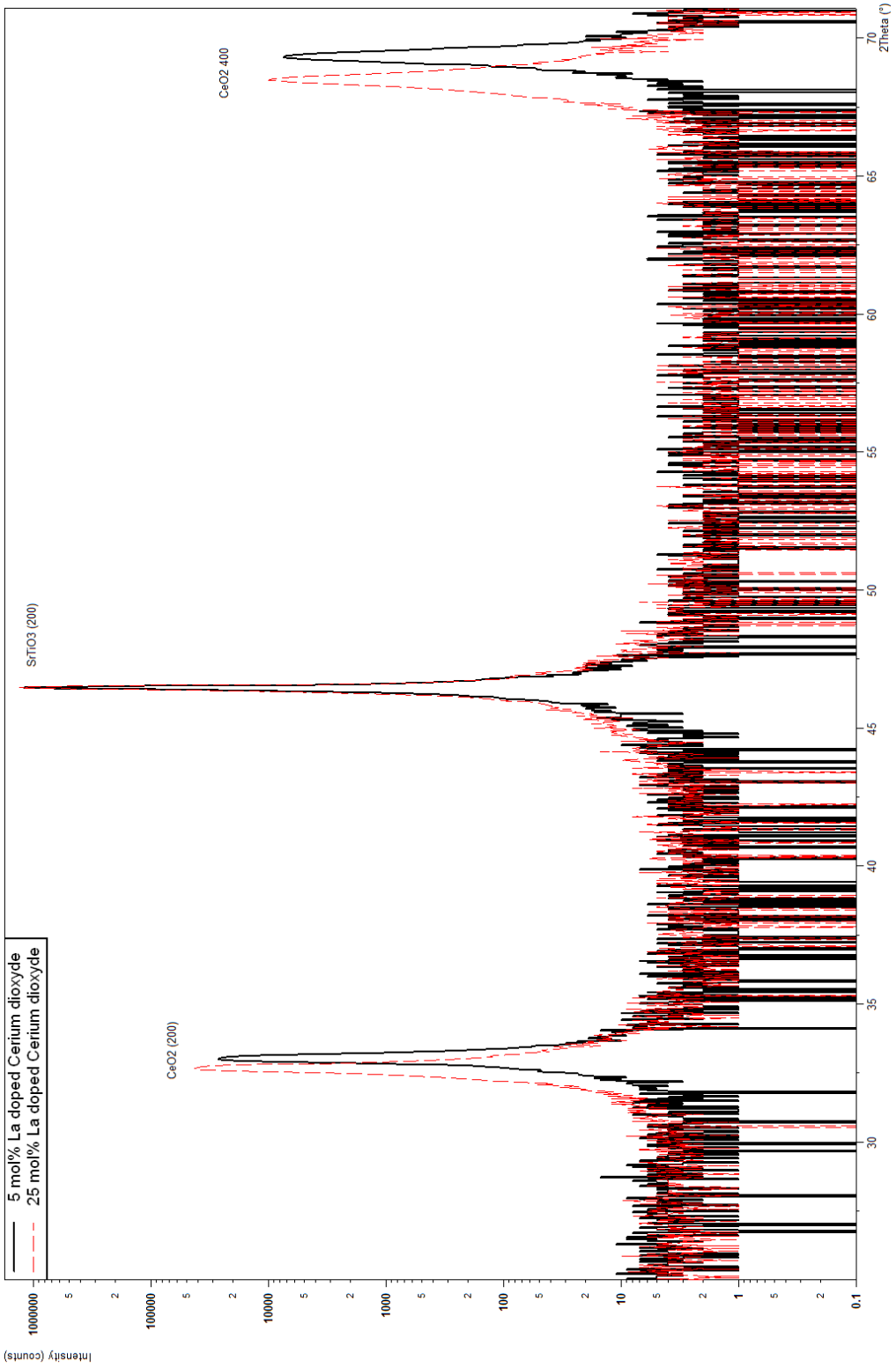

Figure 5.1: XRD θ-2θ analysis on 5mol%(blue curve) and 25 mol%(black curve) La doped CeO_2. The red-dotted curve are from the a pure CeO_2 sample not used in this research

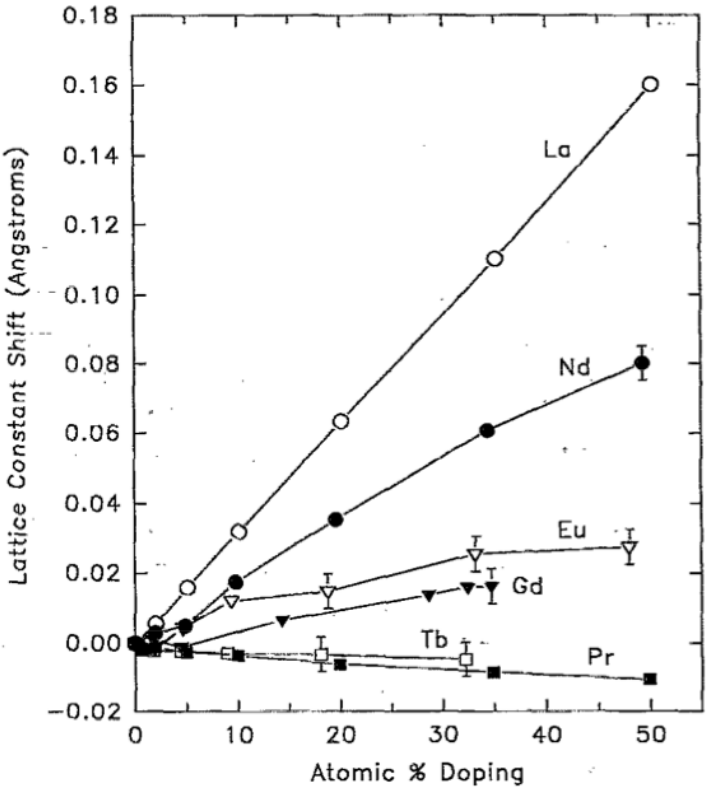

Figure 5.2: Lattice parameter shift from pure CeO_2 for Ce_{1-x}(La, Nd, Eu, Gd, Tb or Pr)$_x O_{2-0.5x}$, samples as measured by XRD.[27]

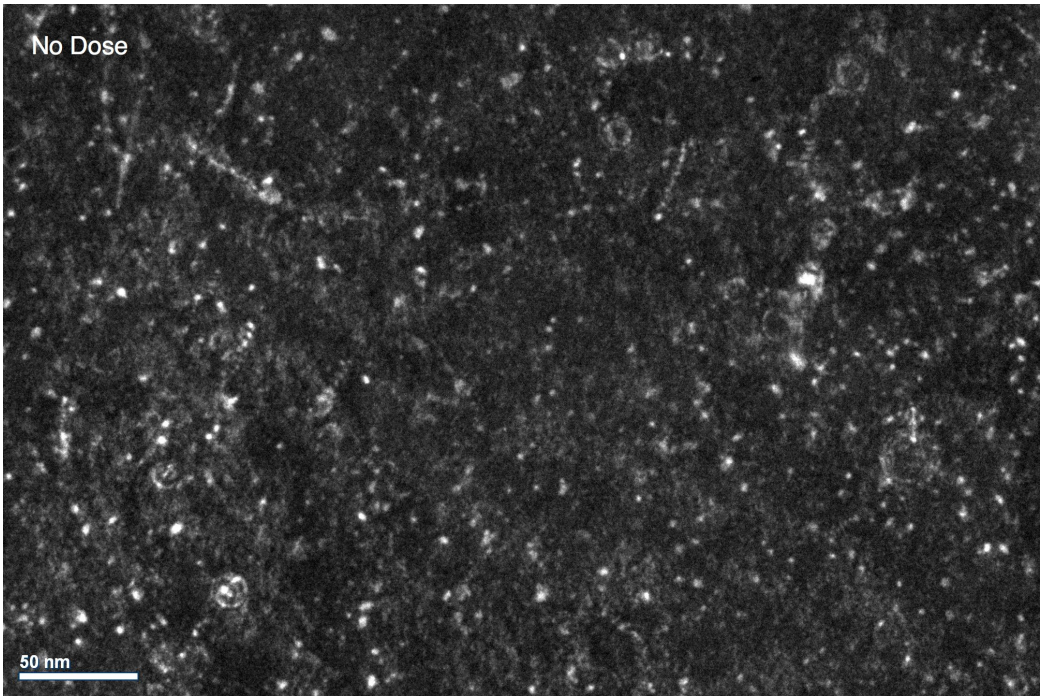

Figure 5.3: Dark field image of 5 mol% La doped CeO_2 before irradiation

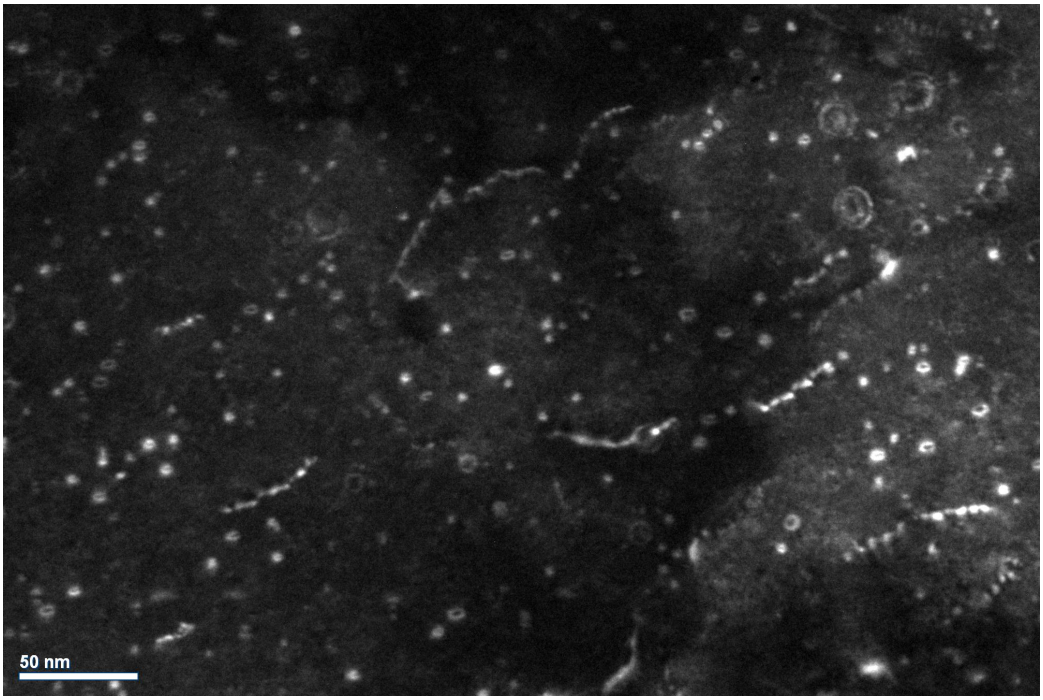

Figure 5.4: Dark field image of 5 mol% La doped CeO_2 at the dose of 5×10^{13} ions/cm^2

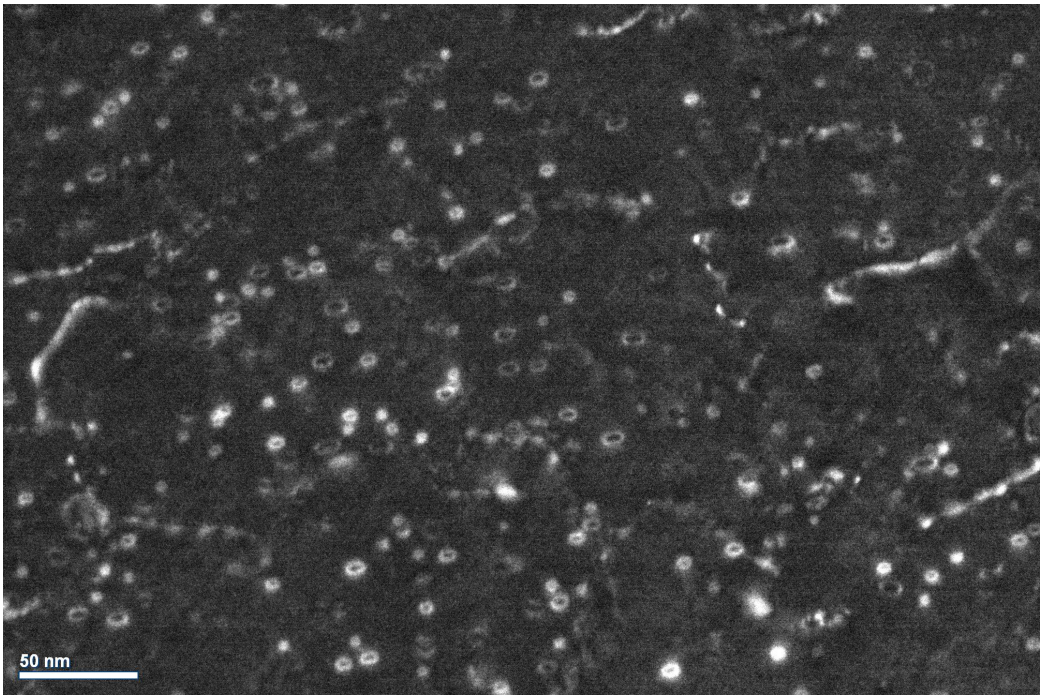

Figure 5.5: Dark field image of 5 mol% La doped CeO_2 at the dose of 1×10^{14} ions/cm^2

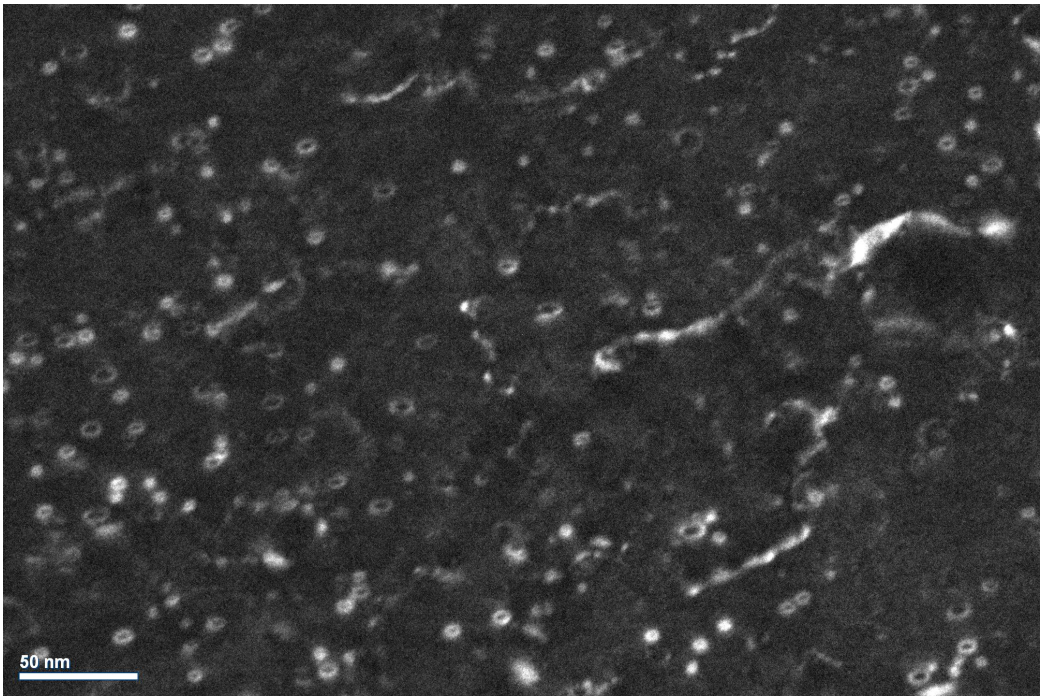

Figure 5.6: Dark field image of 5 mol% La doped CeO_2 at the dose of 3×10^{14} ions/cm^2

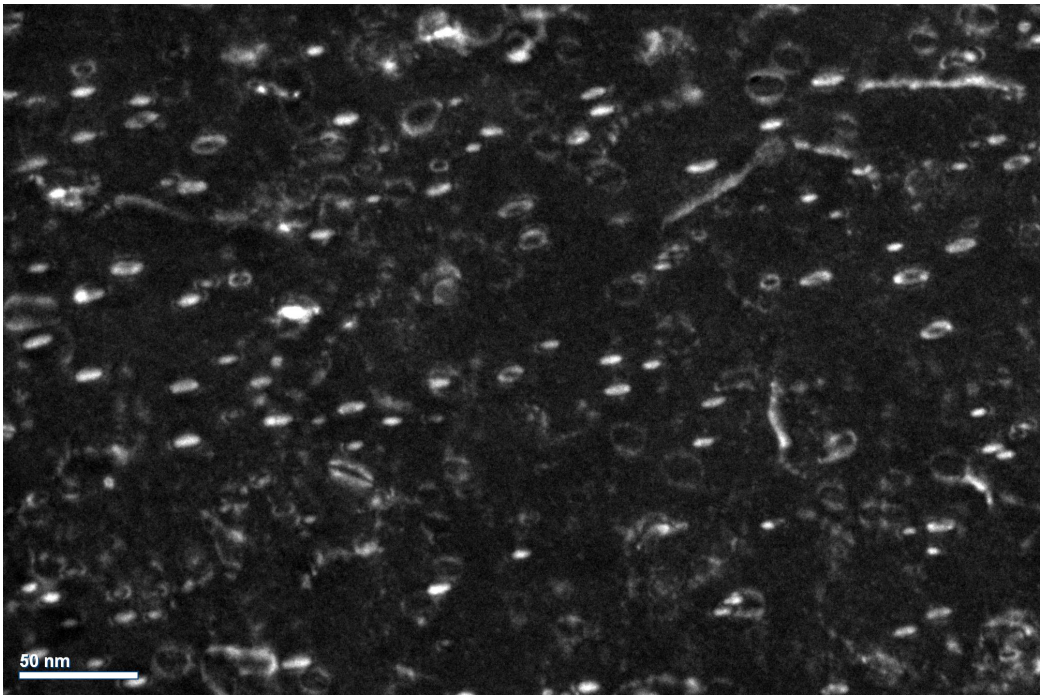

Figure 5.7: Dark field image of 5 mol% La doped CeO_2 at the dose of 5×10^{14} ions/cm^2

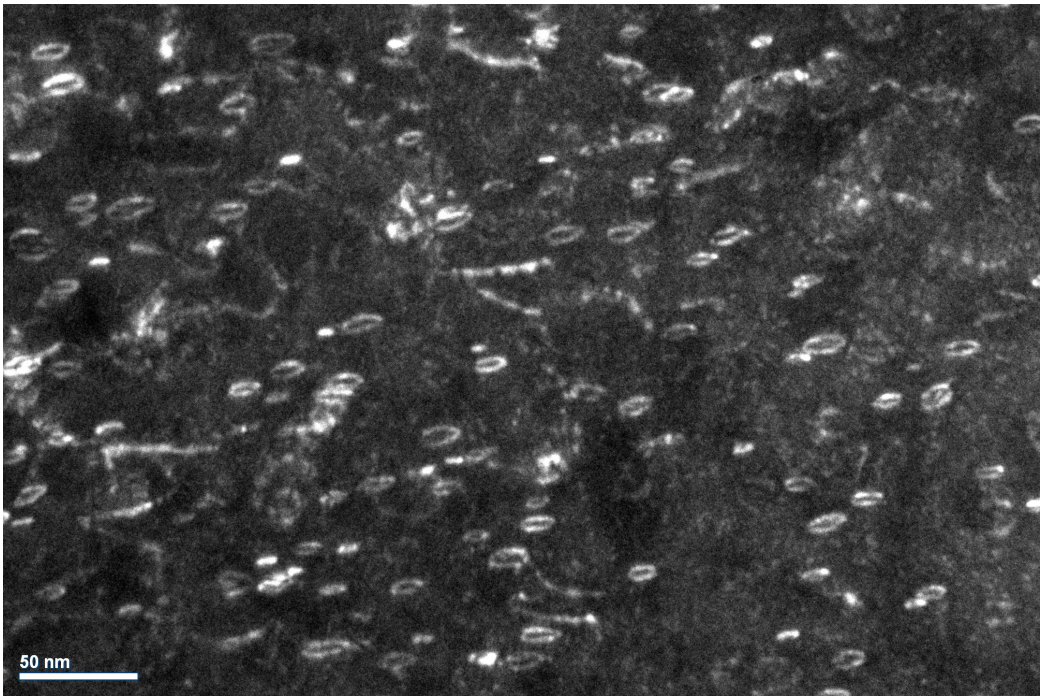

Figure 5.8: Dark field image of 5 mol% La doped CeO_2 at the dose of 8×10^{14} ions/cm^2

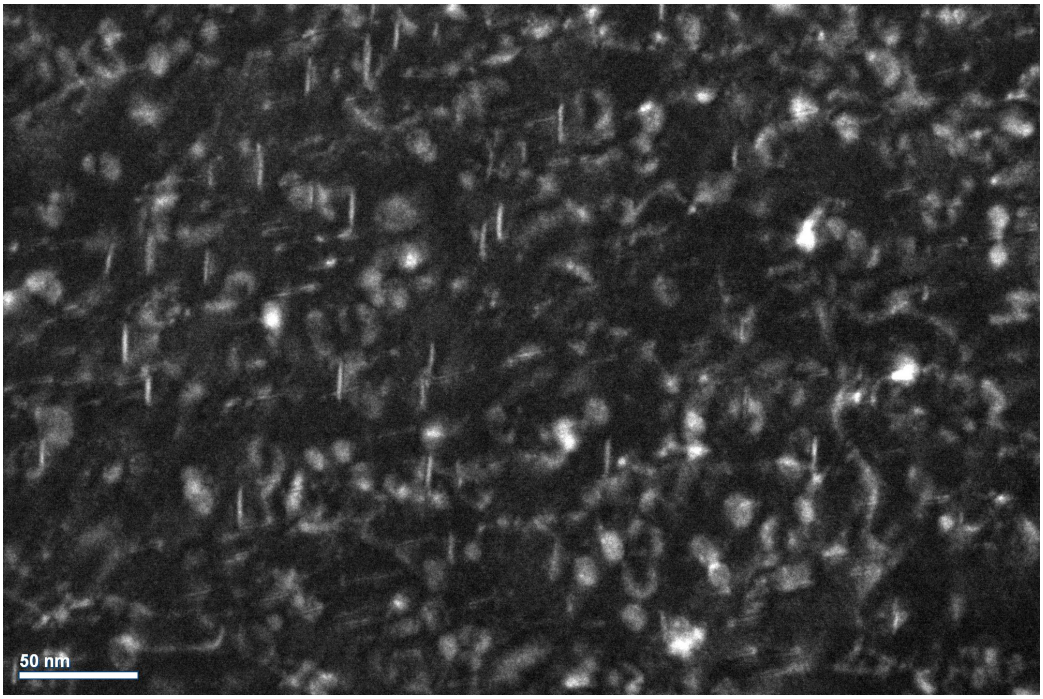

Figure 5.9: Dark field image of 5 mol% La doped CeO_2 at the dose of 1×10^{15} ions/cm^2

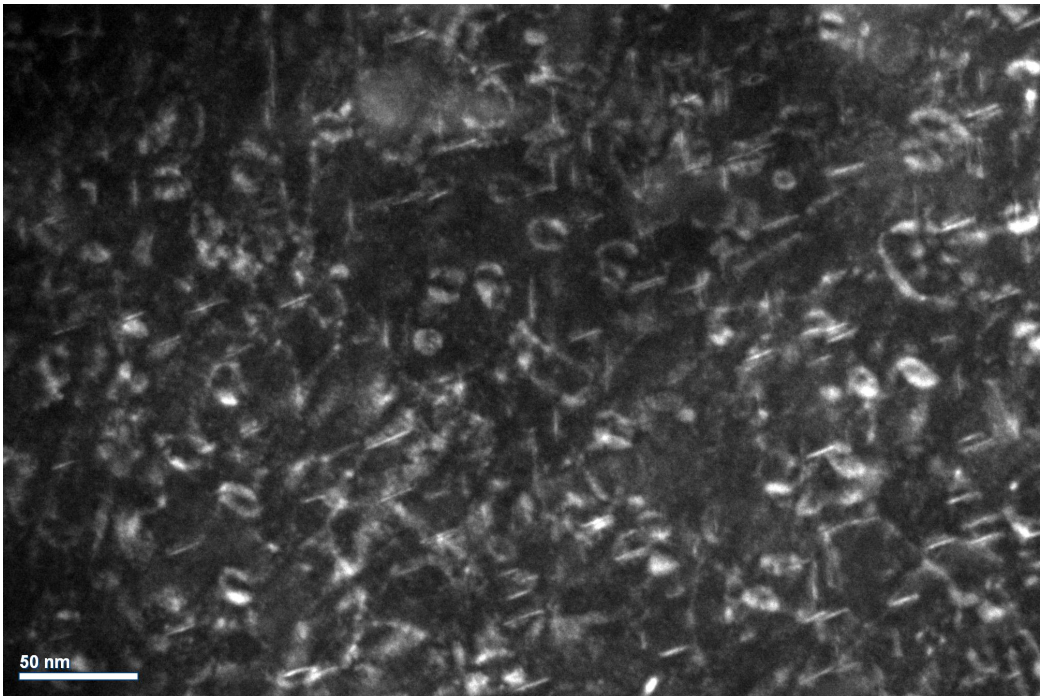

Figure 5.10: Dark field image of 5 mol% La doped CeO_2 at the dose of 1.5×10^{15} ions/cm^2

individual loops to extended dislocation loops networks. Only dislocation loops were clearly observed, which is reasonable because the energetic ions should have penetrated CeO_2 film entirely rather than been implanted inside the film to form bubbles.

Similarly, the *in situ* TEM images from the 25 mol% La doped sample are presented in Figure 5.11 - 5.17 below. At doses 3×10^{14} ions/cm^2 and and 8×10^{14} ions/cm^2 , the diffraction condition was slightly too strong, but those images are still presented here for consistency. Images with higher quality but not in exactly the same area (still nearby) are available in Appendix.

In Figure 5.18, the bright field images corresponding to the dark field images above are cropped and showed. The effects of La on the nucleation and growth of dislocation loops are evident. Summarizing Figure 5.18 and previous work on pure CeO_2 [11], the growth rate of dislocation loops was fastest for the 25 mol% La doped sample and slowest for the 5 mol% La doped sample. Growth rate is slightly faster in pure CeO_2 than the 5 mol% sample.

5.19 Quantitative measurements of average loop size give information about the growth rate of dislocation loops and are shown in Figure 5.19. For all

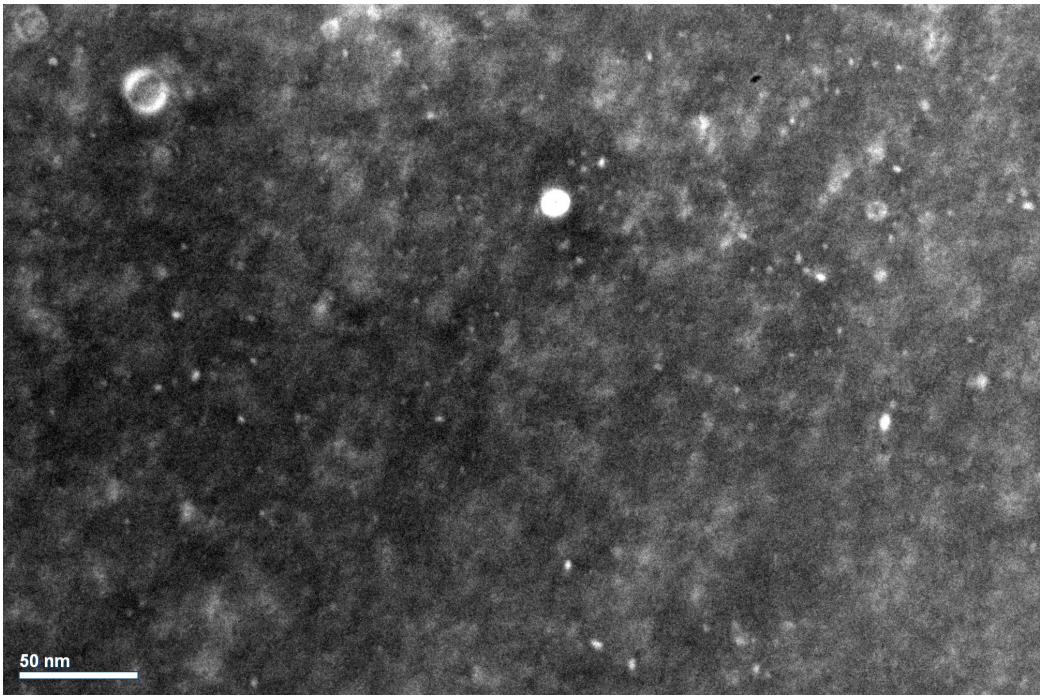

Figure 5.11: Dark field image of 25 mol% La doped CeO_2 before irradiation

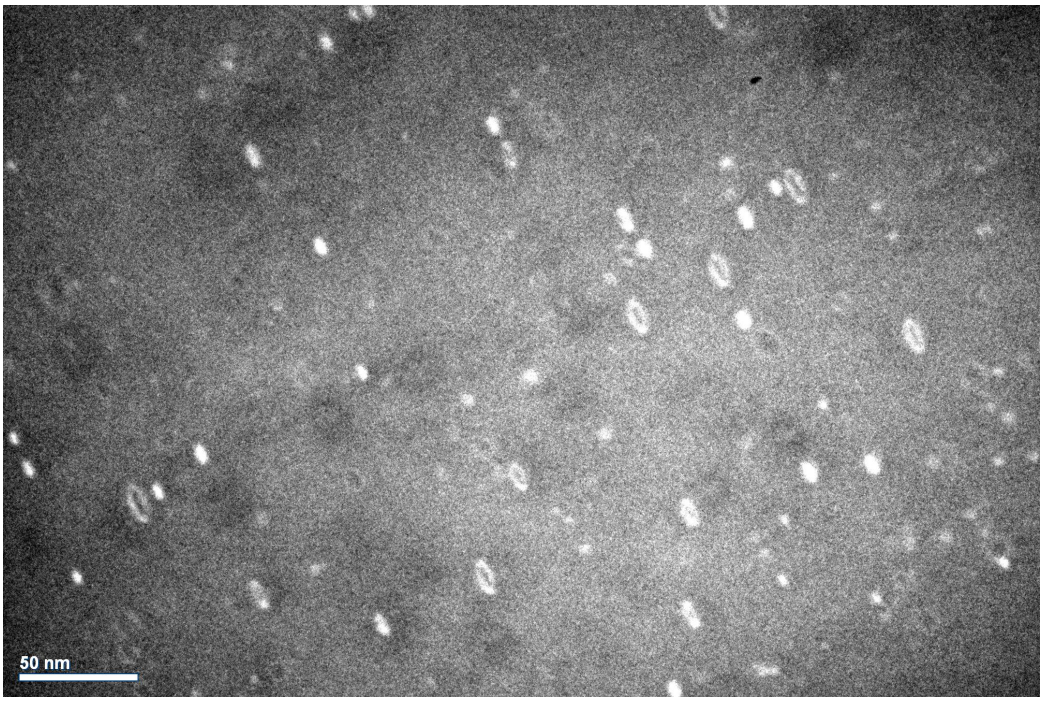

Figure 5.12: Dark field image of 25 mol% La doped CeO_2 at the dose of 1×10^{14} ions/cm^2

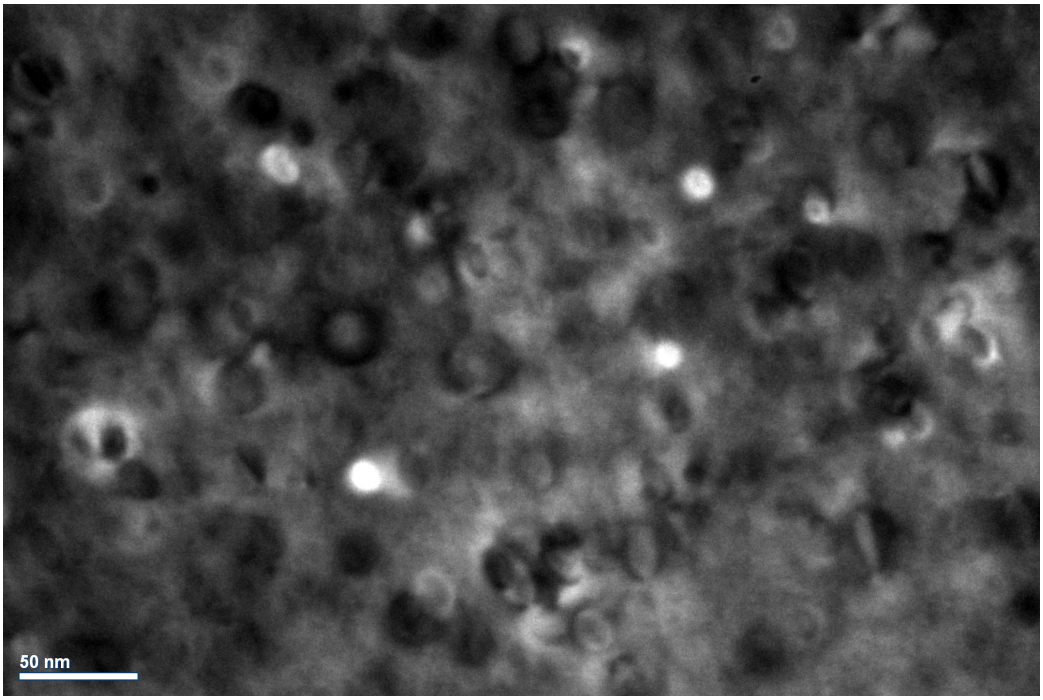

Figure 5.13: Dark field image of 25 mol% La doped CeO_2 at the dose of 3×10^{14} ions/cm^2

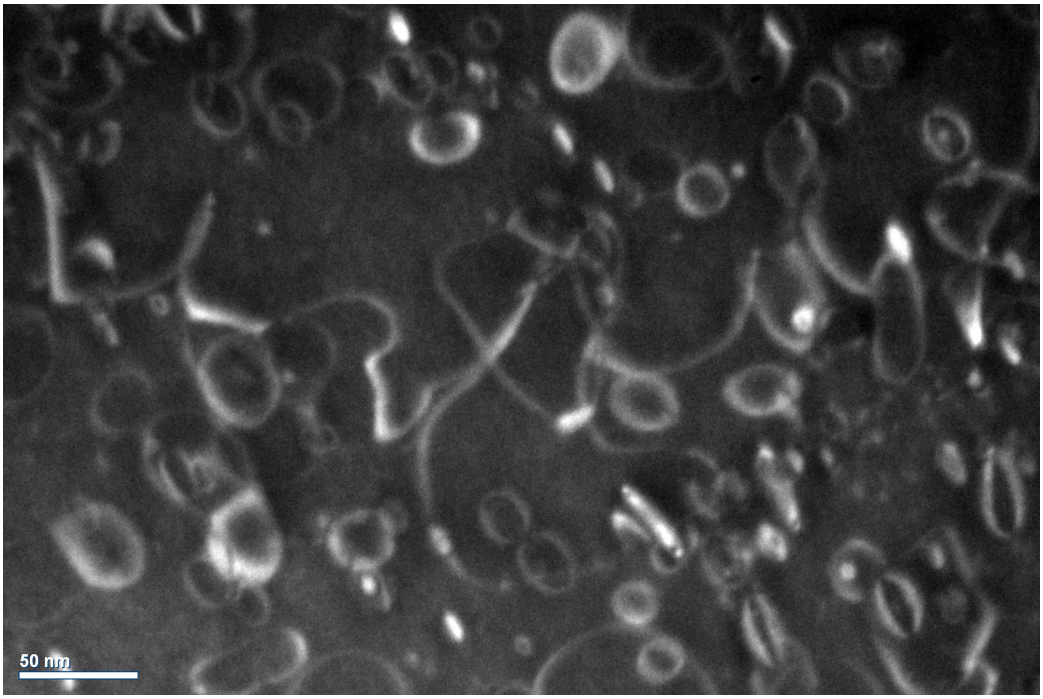

Figure 5.14: Dark field image of 25 mol% La doped CeO_2 at the dose of 5×10^{14} ions/cm^2

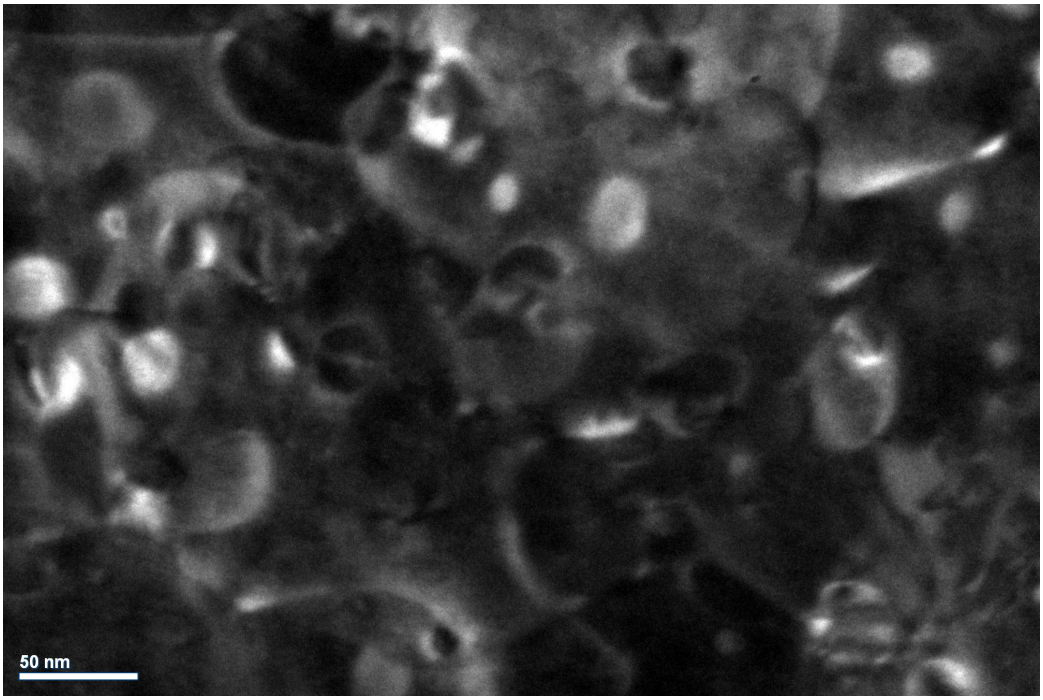

Figure 5.15: Dark field image of 25 mol% La doped CeO_2 at the dose of 8×10^{14} ions/cm^2

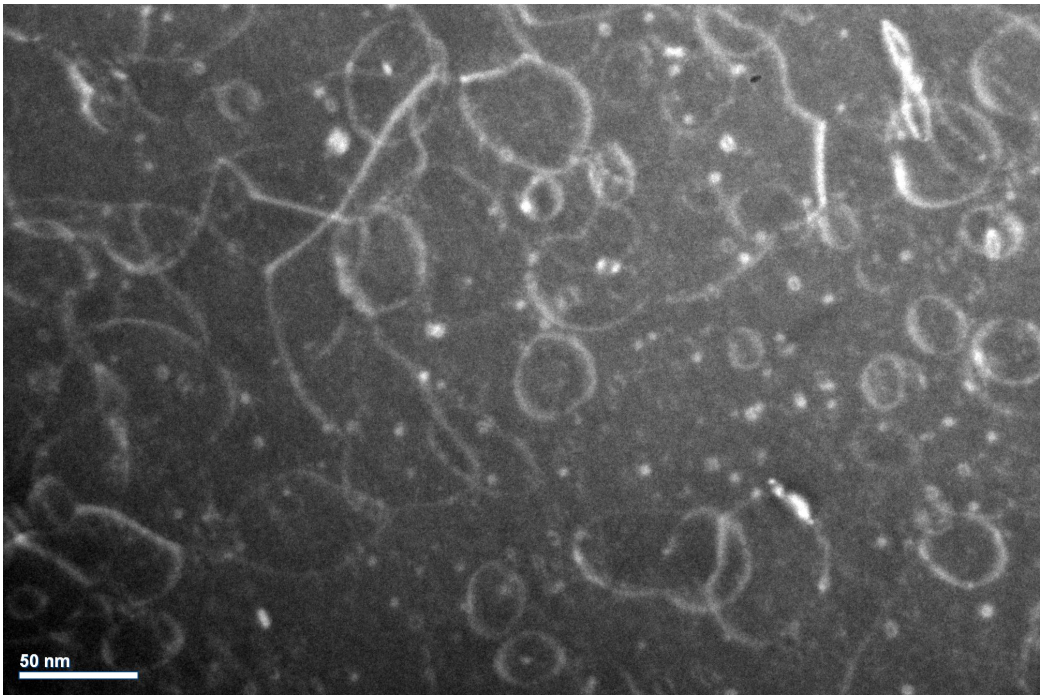

Figure 5.16: Dark field image of 25 mol% La doped CeO_2 at the dose of 1×10^{15} ions/cm^2

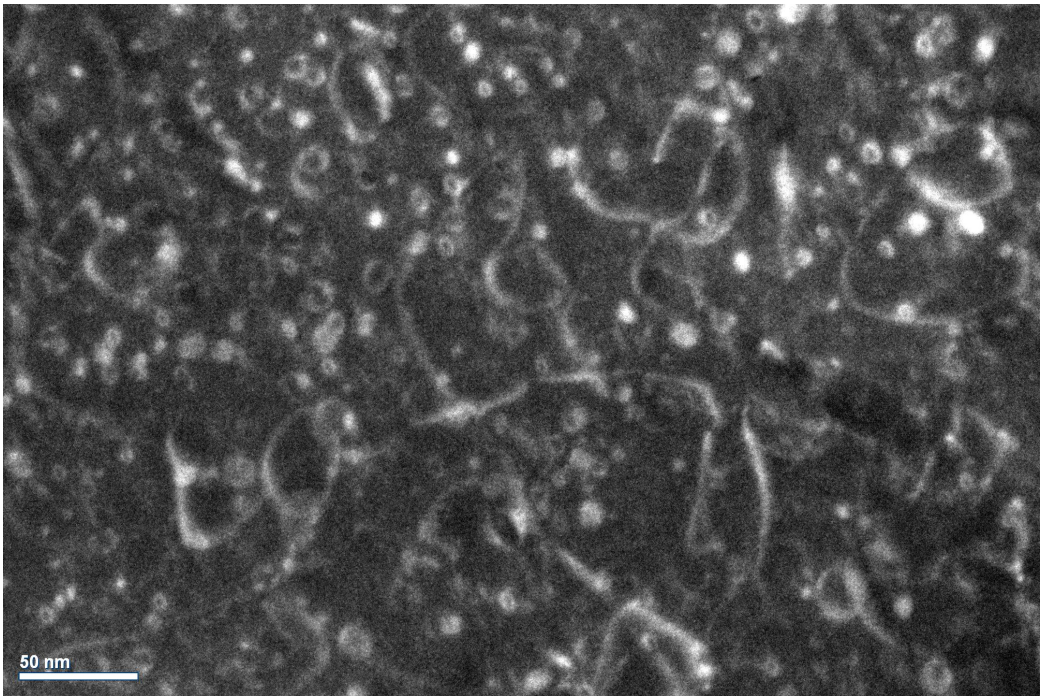

Figure 5.17: Dark field image of 25 mol% La doped CeO_2 at the dose of 1.5×10^{15} ions/cm^2

cases, the average diameter of dislocation loops increases linearly up to dose of 8×10^{14} ions/cm^2 after which the average loop size of 25 mol% sample decreases due to the nucleation of new loops around a dose of 1×10^{15} ions/cm^2 (See Figure 5.16) whereas the 5 mol% and pure samples continued the original linear trend. It should be noted that in the pure CeO_2 sample at 1.5×15 ions/cm^2, some of the large dislocations (-100nm) were cut off by the edge of the image and could not be measured properly. These loops were not included in the estimate of the average loop diameter, which may have resulted in underestimation.This may also have contributed to the size decrease for the 25 mol% sample, but it is not the primary reason for the decrease.

It is difficult to measure the loop density because of the uncertainty of thickness of the area being observed. In addition, a small degree of change in the diffraction condition could make loops invisible and cause them to be overlooked even though every effort was made to maintain the same diffraction condition. It is therefore difficult to compare loop densities from one sample to another.

Nevertheless, with confidence in the understanding on the thickness and diffraction condition, it is believed that the 25 mol% La doped sample has a

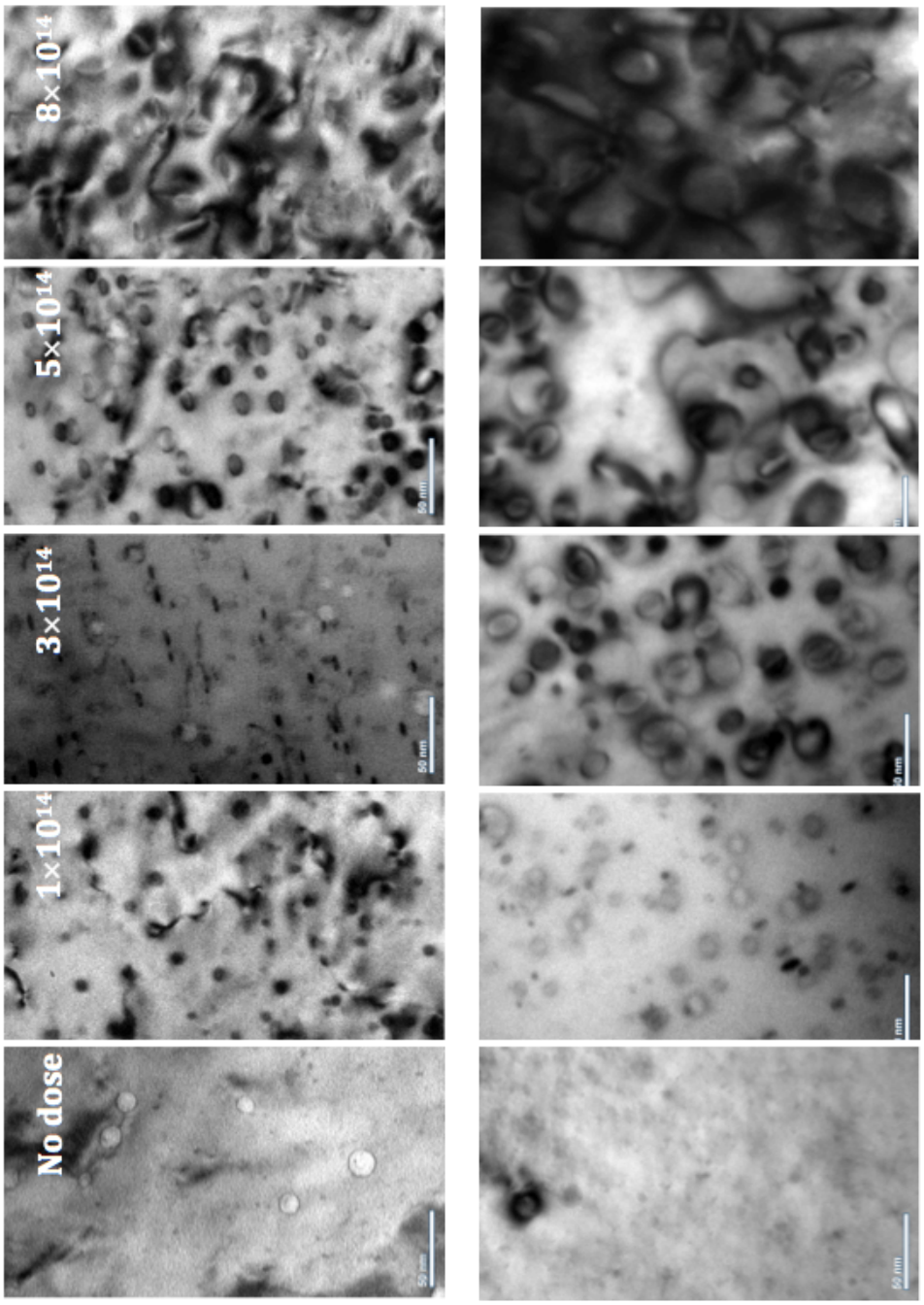

Figure 5.18: Top: Bright field images of sequential change in 5 mol% La doped sample. Bottom: Bright field images of sequential change in 25 mol% doped sample. The dose levels of the bottom images are the same as of the top and not labeled for simplicity.

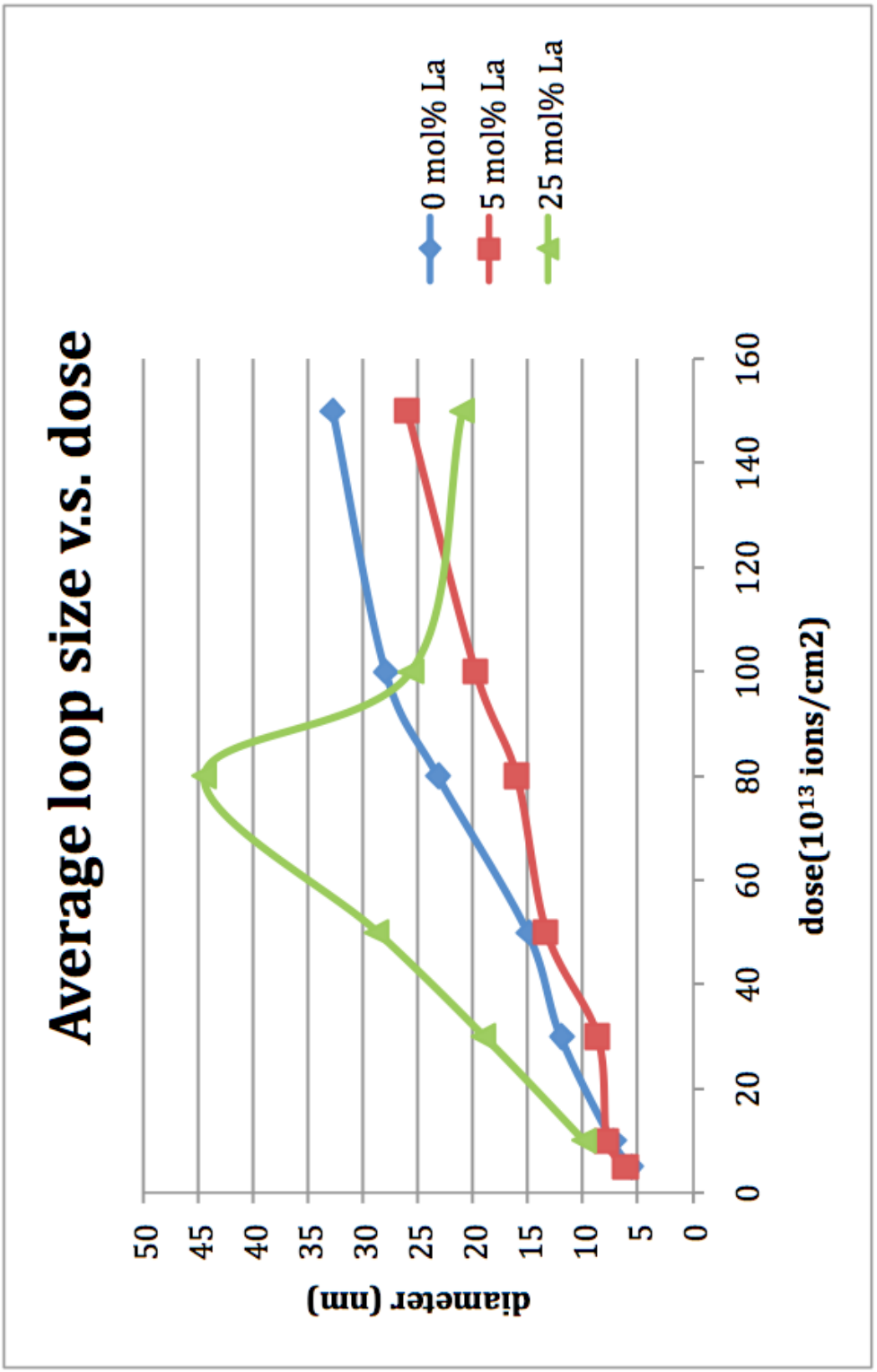

Figure 5.19: The measurement of the relationship between diameter of loops and the dose for pure CeO_2 , 5 mol% and 25 mol% doped CeO_2

smaller loop density than the 5% and pure samples for doses up to 8×10^{14} ions/cm^2.

Several different diffraction conditions were taken in order to clarify the nature of dislocation loops.The results of the different diffraction conditions in the 5 mol% sample at a dose of 1.5×10^{15} ions/cm^2 are shown in Figure 5.20. Of special interest is Figure 5.20 (C), as it shows an edge-on feature of dislocation loops. The angle between those edge-on features is around 70 degrees which is close to the angle between two {111} planes on the [110] zone. In order to confirm that those edge-on loops are indeed dislocation loops on {111} planes, images were firstly matched with diffraction pattern. As showing in Figure 5.21 (A) and (B), the edge-on contrast is perpendicular to {111} directions, thus it lies on {111} planes. Additionally, Figure 5.21 (C) and (D) showing the images near the [110] pole direction and away from the [110] pole direction proves that the edge-on contrast is from dislocation loops.

On the contrary to the images from the [110] pole direction, no edge-on dislocation loops were found on [100] planes as in Figure 5.20 (A). This observation indicates that no dislocation loops reside on {220} or {200} planes.

Despite the confirmation of {111} loops and no {220} and {200} loops, this does not exclude the possibility for loops to exist on other planes. Some very large loops observed in other diffraction conditions, like the ones in Figure 5.20 (A) (B), do not appear as the edge-on loops when the beam is at [110] direction as in Figure 5.20 (C), which means those very large loops are on planes other than {111}.

Stacking-fault-like fringes were observed in the 5 mol% La doped samples as shown in Figure 5.22 to 5.23. The contrast with parallel lines inside is very similar to the precipitation and stacking fault. Two type of these features were observed: facet shape (as showed in Figure 5.22) and oval shape (As shown in Figure 5.23). The facet-shaped contrast was firstly observed coexisting with the oval-shaped contrast for the first 5 mol% La sample examined at the dose of 1×10^{15} ions/cm^2 but not were never observed again at different doses or other samples. On the contrary, the oval-shaped contrast could be reproduced at different doses and multiple samples.

Unfortunately the diffraction condition used was not recorded during the *in-situ* experiments in ANL. However, the sample were examined later *ex situ* in MRL in UIUC with a Lab6 TEM and it turned out that these stacking

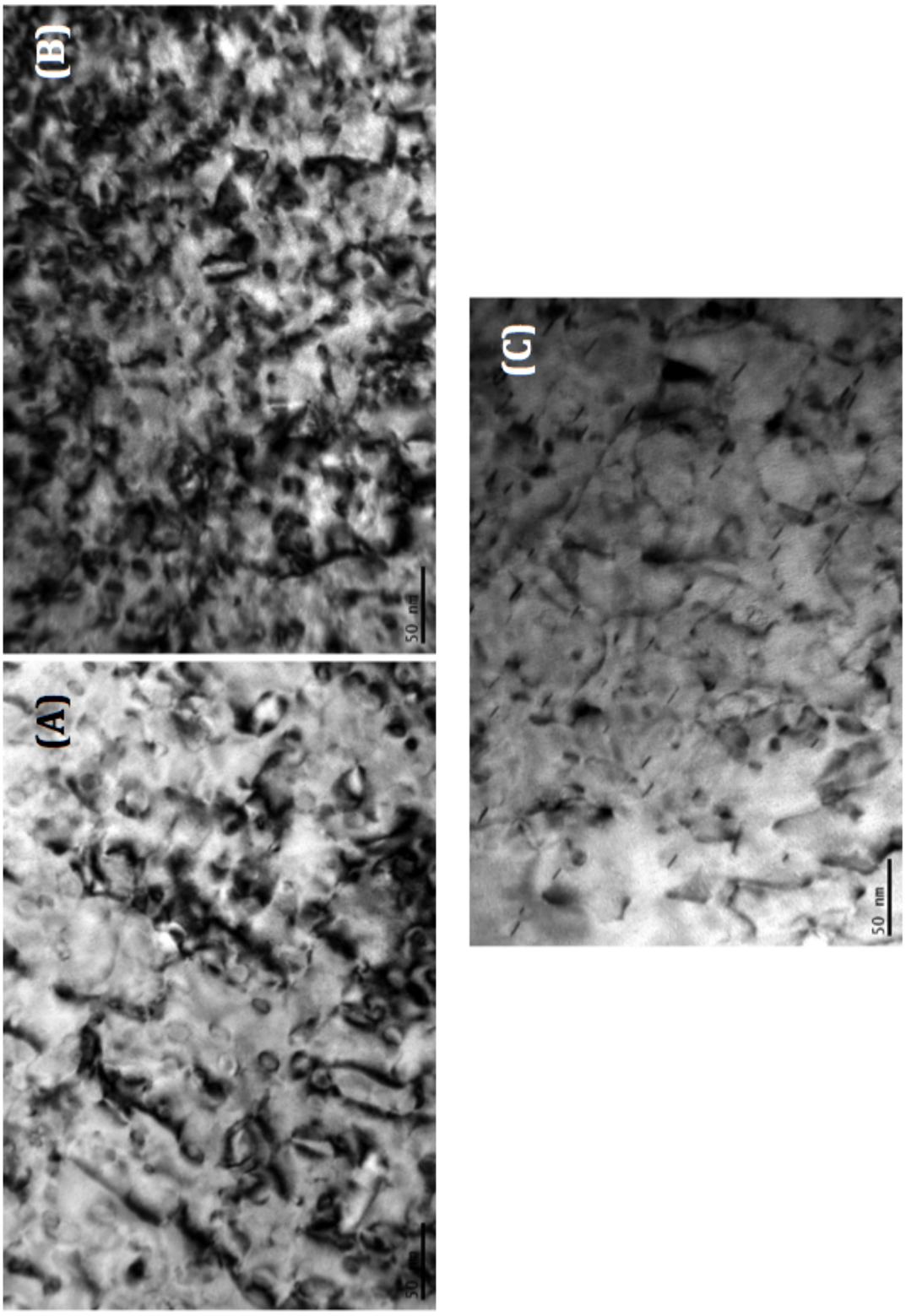

Figure 5.20: Micrographs of 5 mol% La doped sample taken at dose of 1.5×10^{15} ions/cm^2 in diffraction condition (A) g = 220 at [001] direction (B) g = 220 at [1-11] direction (C) g = 200 at [011] direction

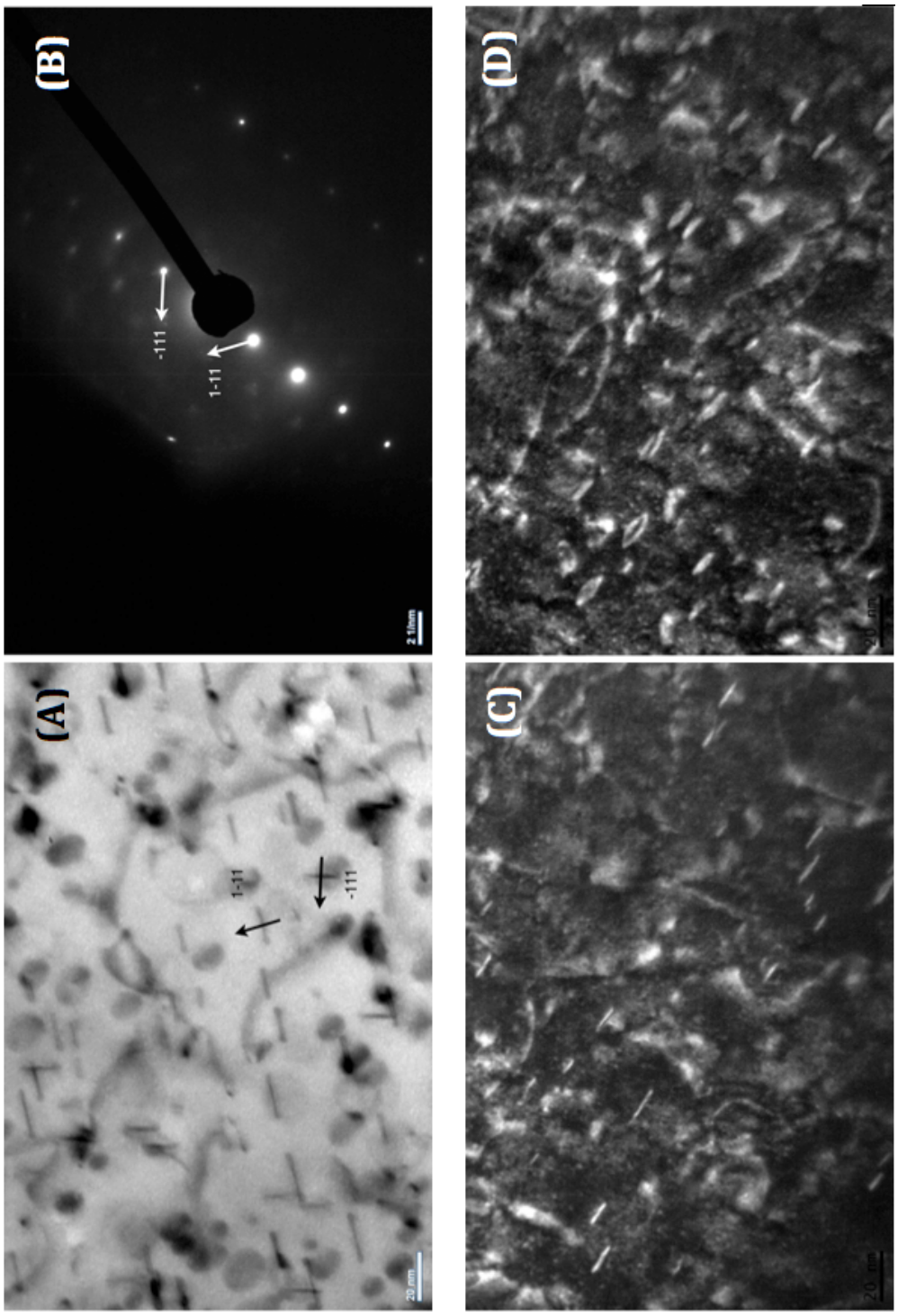

Figure 5.21: (A) Bright field image of sample A at the dose of 10×10^{15} ions/cm^2 with g = (002) at [110] direction. (B) The diffraction pattern corresponding to (A). (C) Dark field image of sample A at the dose of 1.5×10^{15} with g = (002) at [110] direction. (D) Dark field image of the nearby area of (C) after a rotation of the sample about [001] axis.

fault features would appear in the diffraction condition of g = (111) at [112] direction (Figure 5.24) but not on other major diffraction conditions used in this study (for instance, Figure 5.20).

The size distribution of these stacking fault loops is similar to the dislocation loops appearing with the diffraction condition of g = (200) at [011] direction. One conjecture would be that those stacking fault loops are the same loops as before but having different contrast because of distinct diffraction condition. However, it's also possible that they are something different like dislocation loops with a different nature or precipitates. Further study is required to understand them.

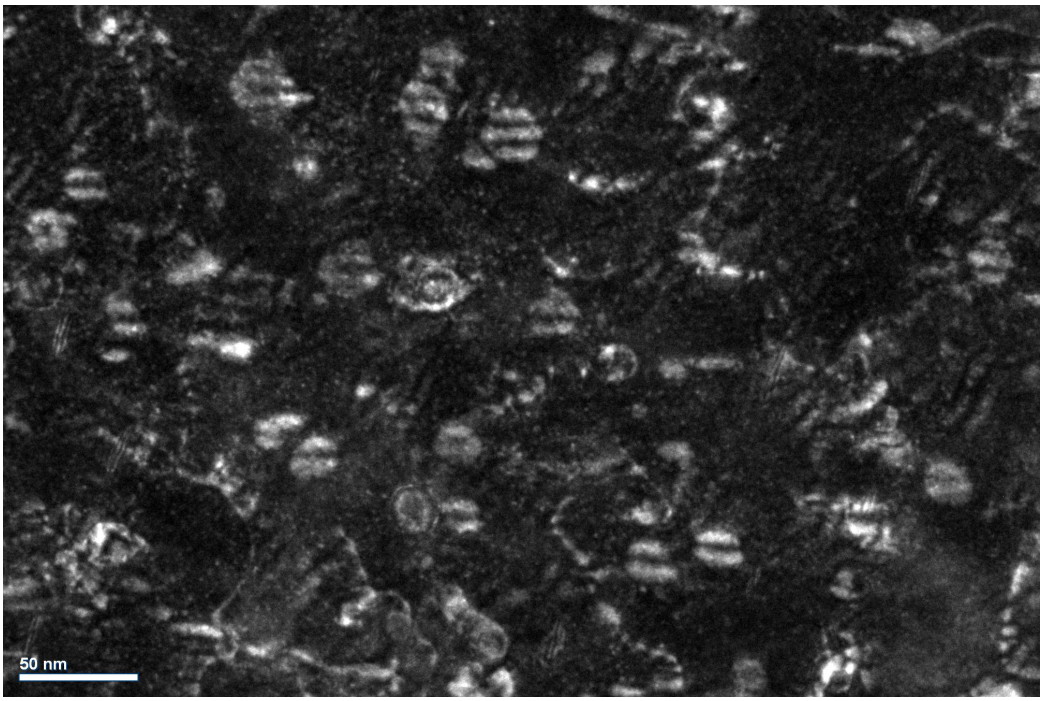

Figure 5.22: Dark field image of 5 mol% La doped CeO_2 at the dose of 1×10^{15} ions/cm^2 with magnification equal to $\times$60k

5.3 Discussion About the Nature of the Loops

As in Figure 5.21, the loop plane was determined to be {111} plane. This is in accordance with previous work with high energy electron irradiation [4]. Burger's vector was determined to be along [111] direction earlier by Di Yun and Bei Ye [22] which is also in accordance with the results from

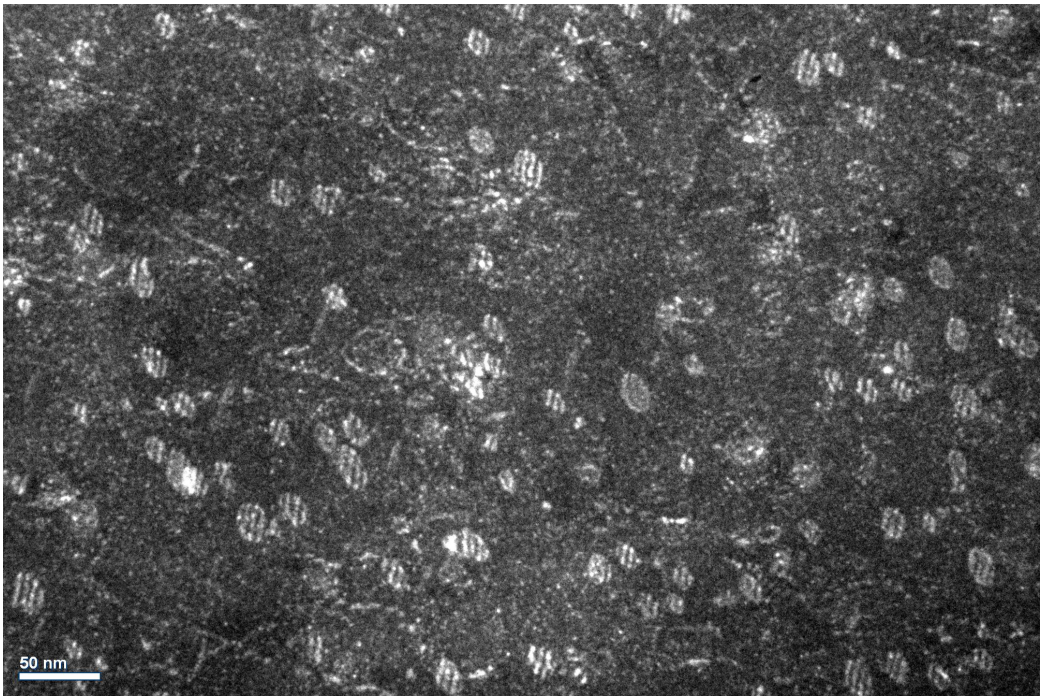

Figure 5.23: Dark field image of 5 mol% La doped CeO_2 at the dose of 1×10^{15} ions/cm^2 with magnification equal to $\times$40k.

Yasunaga et al. As was mentioned earlier in the Chapter 1, Yasunaga et al. claimed the loops are believed to be of interstitial type and are claimed to be composed of oxygen interstitials alone. However, this configuration is doubtful because a clustering of oxygen interstitials without the participation of cerium interstitials would inherently have high potential energy from oxygen ions repulsion. Although Shiiyama et al. reported a clustering of oxygen interstitials on {111} plane by MD calculation [10], Miao showed that the clustering of pure oxygen interstitials are thermaldynacially prohibited [28]. The binding energy of the oxygen interstitial cluster is calculated by subtracting the defect energy of the system with clustered interstitials from that of the system with isolated interstitials. The results are listed in Table 5.1. The positive binding energy indicate that oxygen interstitials disfavor clustering.

A more convincing configuration of dislocation loops is found by D.S. Aidhy through MD simulation [29]. As showed in Figure 5.25, dislocation loop contain a three layer of interstitial structure (O-Ce-O) with a thickness of a regular {111} inter-planar distance.

This configuration of dislocation loops is more energetically reasonable due

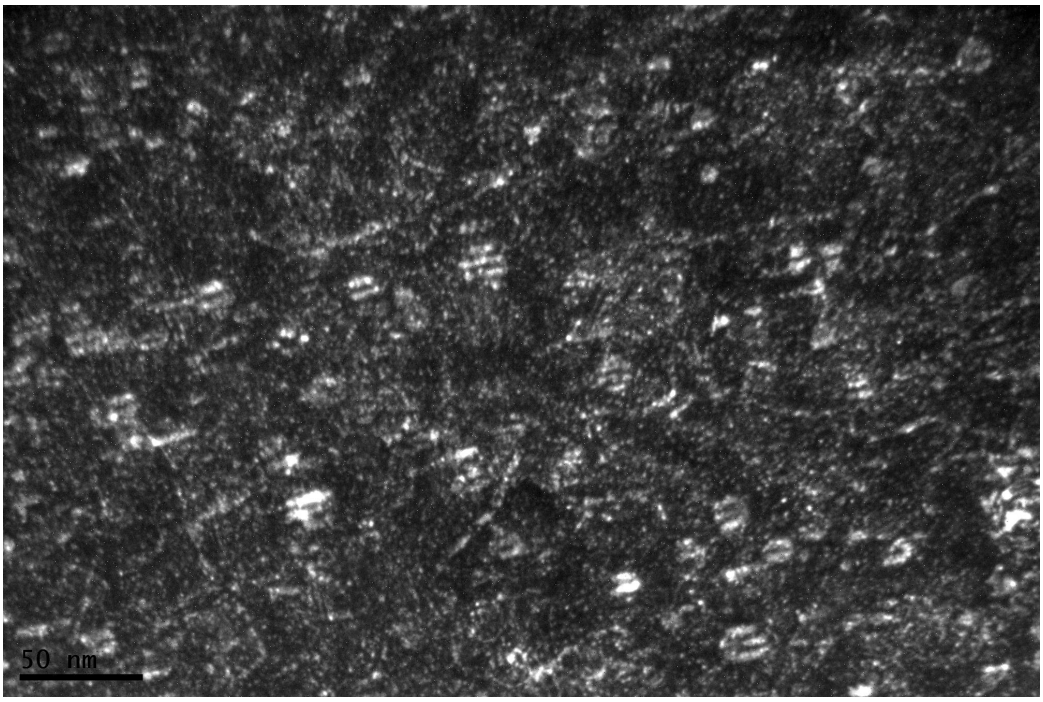

(a) Image

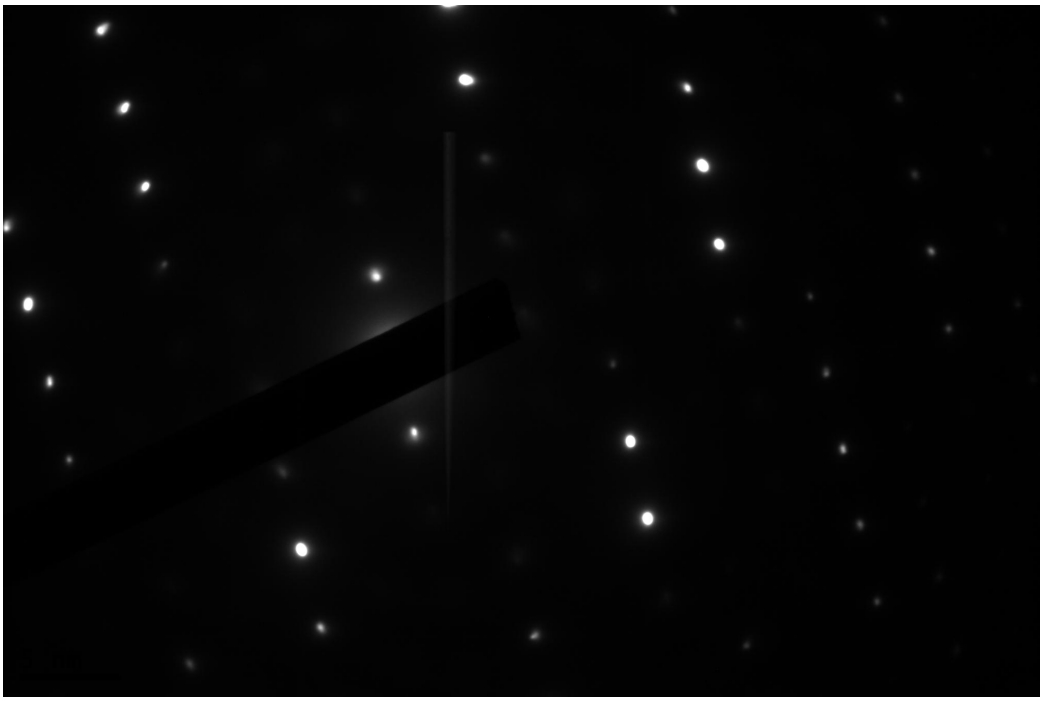

(b) Diffraction patern

Figure 5.24: (a)Dark field image of 5 mol% La doped CeO_2 at the dose of 1.5×10^{15} ions/cm^2 with magnification equal to $\times$60k and (b) the corresponding diffraction pattern showing the diffraction condition to be g = (111) at $[11\bar{2}]$ direction

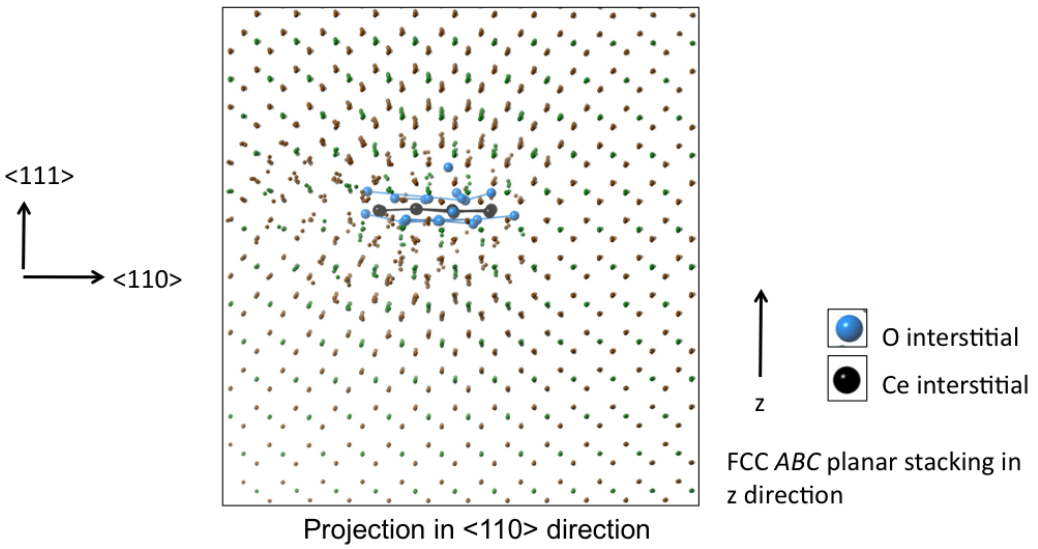

Figure 5.25: Formation of a dislocation loop composed of both oxygen interstitials and cerium interstitials. Results from D. S. Aidhy et al. [29]

to charge balance. However, more detailed experiments have to be conducted to confirm it.

5.4 Dependence of Loop Growth Rate on La Concentration

The growth rate of dislocation loops in CeO_2 for different La concentrations was calculated by least squares method on the average measured size (as showed in Figure 5.19) and the results are presented in Table 5.2. Data points for 25 mol% La curve after 8×10^{14} ions/cm^2 were excluded because the drop in average loop size was caused by nucleation of new tiny loops. The last data point of the curve for pure CeO_2 was also ignored because it was underestimated when large loops cut by the image edge were not counted.

The complexity resides in that the loop growth rate decreased with slight

Table 5.1: Binding energy calculation of oxygen interstitials clustering . Energies are in eV.

Type - Potential	Minervini	Gotte	Shiiyama
Di-interstitials	1.473	0.54	0.835
Quad-interstitials	4.766	3.285	2.361

increase in La concentration (5 mol% sample), but then substantially increased when concentration of La was further increased (25 mol% sample). Since several competing mechanisms control the growth of dislocation loops, there is a turning point in the curve of growth rate. Those mechanisms are related to point defect kinetics, which can be expressed approximately by a set of differential equations firstly proposed by Hayns [30]:

$$\frac{dc_v(t)}{dt} = K - \alpha_r c_v(t) c_i(t) - \sum_{n=2}^{neq} L_n c_{ni}(t) c_v(t) - D_v \rho_d c_v(t)$$

$$\frac{dc_i(t)}{dt} = K - \alpha_r c_v(t) c_i(t) - K_2 c_i(t) c_i(t) - \sum_{n=2}^{neq-1} R_n c_{ni}(t) c_i(t) + L_2 c_{2i}(t) c_v(t) - D_i \rho_d c_i(t)$$

$$\frac{dc_{2i}(t)}{dt} = \frac{1}{2} K_2 c_i(t) c_i(t) + L_3 c_{3i}(t) c_v(t) - L_2 c_{2i}(t) c_v(t) - R_2 c_{2i}(t) c_i(t)$$

$$\frac{dc_{3i}(t)}{dt} = R_2 c_{2i}(t) c_i(t) + L_4 c_{4i}(t) c_v(t) - L_3 c_{3i}(t) c_v(t) - R_3 c_{3i}(t) c_i(t)$$

.... and so on.

The equations above were proposed to describe how the interstitial loops evolve during irradiation in graphite and steel. α_r is the vacancy-interstitial annihilation rate. K is the rate of point defect being created by irradiation. D_v and D_i are the diffusivity of vacancies and interstitials respectively. c_v and c_i are the concentration of vacancies and interstitials respectively. ρ_d is the sink density. c_{ni} is the concentration of loop composed of n interstitials. L_n and R_n are the reaction rate of loop of size n to increase or decrease in size.

For the case of CeO_2, we need to consider both Ce ions and O ions. So

Table 5.2: Growth Rate of Dislocation Loops

% La in CeO_2	Effective La in CeO_2	Growth Rate (nm/(10^{14} ions/cm2))
0	0	2.3
5	3.5	1.35
25	22	4.9

the governing equations will be more complex by including more terms. It's not the purpose for this study to numerically solve these equations but to have a sense of what factors are controlling the growth of dislocation loops. Through studying the above equations, several factors were considered: the annihilation rate and diffusivity.

5.4.1 Annihilation Rate

The average growth rate of interstitial dislocation loops depends on the availability of interstitials. D. Aidhy et al. illustrated that interstitials would cluster faster when vacancies are immobile [13]. When vacancies are deterred from annihilating interstitials, interstitials are more likely to cluster and grow.

Molecular static (GULP [31]) and dynamics (LAMMPS [32]) simulations were done with Yinbin Miao to determine the effect of La on the annihilation process. Table 5.3 shows the statics calculation results for the defect energy of oxygen Frenkel pairs in CeO_2. Depending on the distance between vacancy and interstitial, the pair is categorized as first nearest neighbor (1nn), second nearest neighbor(2nn) and so on. Also, depending the relative position of oxygen vacancy, interstitial and La ion, there can be several possible initial configurations for each group. An N/A means that there is no such configuration and a dash, '-', means there is such a configuration but its defect energy is not yet calculated.

The results show that oxygen Frenkel pair will either annihilate directly (with defect energy close to zero) or have a positive defect energy, which means the vacancy and interstitial will always recombine regardless of the La ions. After validating the tendency of annihilation, MD calculations were used to study whether the presence of La ions accelerate or decelerate the annihilation process. Table 5.4 shows the time required for oxygen interstitial

Table 5.3: Defect Energy of Oxygen Frenkel Pair with La impurity (eV)

Pair Distance	Configuration 1	Configuration 2	Configuration 3
1 nn	0	0	N/A
2 nn	-0.0027	0.0023	6.6242
3 nn	6.5958	7.4412	6.9450
4 nn	7.1554	7.0896	-

and vacancy to recombine under different configurations. The data shows that the presence of La might enhance as well as deter the annihilation process depending if La impurity is positioned in the way.

Since both of the competing results from La exist, the effect of La on the rate of oxygen Frenkel pair annihilation could not be concluded. Cerium Frenkel pairs were not simulated because they hardly move in the scale of MD simulation. Although MD simulations did not give conclusive answers to the La effect on oxygen Frenkel pair annihilation, it is worth noting the process of annihilation. It has been observed that the oxygen vacancy migrates all the way to the oxygen interstitial while the interstitial remains immobile until the vacancy has approached the nearest neighbor site. The interstitial will then jump in and annihilate with the vacancy. This results is similar to MD calculations performed by Shiiyama et al. [10]. This observation implies that it is oxygen vacancies, instead of oxygen interstitials, that are more sensitive to the presence of La ions.

The effect of La on the migration of cerium interstitials and vacancies is unknown because of the lack of data. Despite the immobility of cerium point defects, it could be an important factor controlling the growth rate of dislocation loops, since the slowest factor is usually the controlling factor under the assumption that loops are composed of both cerium interstitials and oxygen interstitials. Thus an understanding of the migration of cerium point defects is necessary and will be one of the major focuses of future work.

5.4.2 Diffusivity of Point Defects

The diffusivity of the point defects are considered here because of its influence on annihilation rate (as is discussed in Section5.4) and the rate of point defects being absorbed by dislocation loops. The addition of La in CeO_2 has two effects on the diffusivity of oxygen vacancies. On one hand, since

Table 5.4: Duration for Oxygen Frenkel pair to annihilate (ps)
with/without the presence of La

Pair Type / Configurations	no La	1	2	3
1 nn	0.070	0.060	0.077	N/A
2 nn	0.184	1.009	0.192	0.791
3nn	1.072	0.471	5.846	0.517

the charge of La is 3+ but that of Ce is 4+, the increasing concentration of La in CeO_2 must increase the concentration of oxygen vacancies in order to maintain charge neutrality. On the other hand, La traps the oxygen vacancies by having a negative binding energy [18] and thus would decrease the its diffusivity. The two competing mechanism results in a maximum in oxygen vacancy diffusivity at around 4 mol% La. This fact has long been known from the measurement on the conductivity dependence of CeO_2 on concentration of La [19].

Besides experiments, computer simulation has also been done to simulate this diffusivity dependence on the concentration of La. Oaks et al. used Kinetic Monte Carlo to simulate the migration and clustering process of oxygen vacancies in CeO_2 under the presence of La ions and the results comply the experiments [25]. The KMC results using the Gotte potential[26] are plotted in Figure 5.26. Diffusivity at x = 0.25 is not plotted here in order to make the peak around x = 0.03 be showed clearly. Values of diffusivity of oxygen vacancies (D_{O_v}) at selective concentration of La are presented in Table 5.5.

By comparing D_{O_v} and the growth rate of loops, the growth rate is observed to be inversely correlated to the diffusivity of oxygen vacancies. It is suspected that the diffusivity of oxygen vacancies is the dominant factor that controls the growth rate of loops. However, lacking microscopic evidence on how they affect changing the rate of growth, no solid conclusions can be drawn. Oxygen interstitials and cerium interstitials are actually thought to be more important because they are the actual components that constitute the loops. In addition, they migrate much more slowly than oxygen vacancies so they are more likely to be the controlling factors.

In sum, the inverse-correlation of D_{O_v} and the growth rate is found but

Table 5.5: KMC Results for Diffusivity of Oxygen Vacancies in CeO_2

La concentration (mol %)	O_v Diffusivity(cm^2/s)	Growth Rate of Dislocation Loop($nm/(10^{14}$ ions/cm^2)
0	2.186	2.3
3.3	2.84	1.35
5	2.596	N/A
22	0.43	4.9
25	0.386	N/A

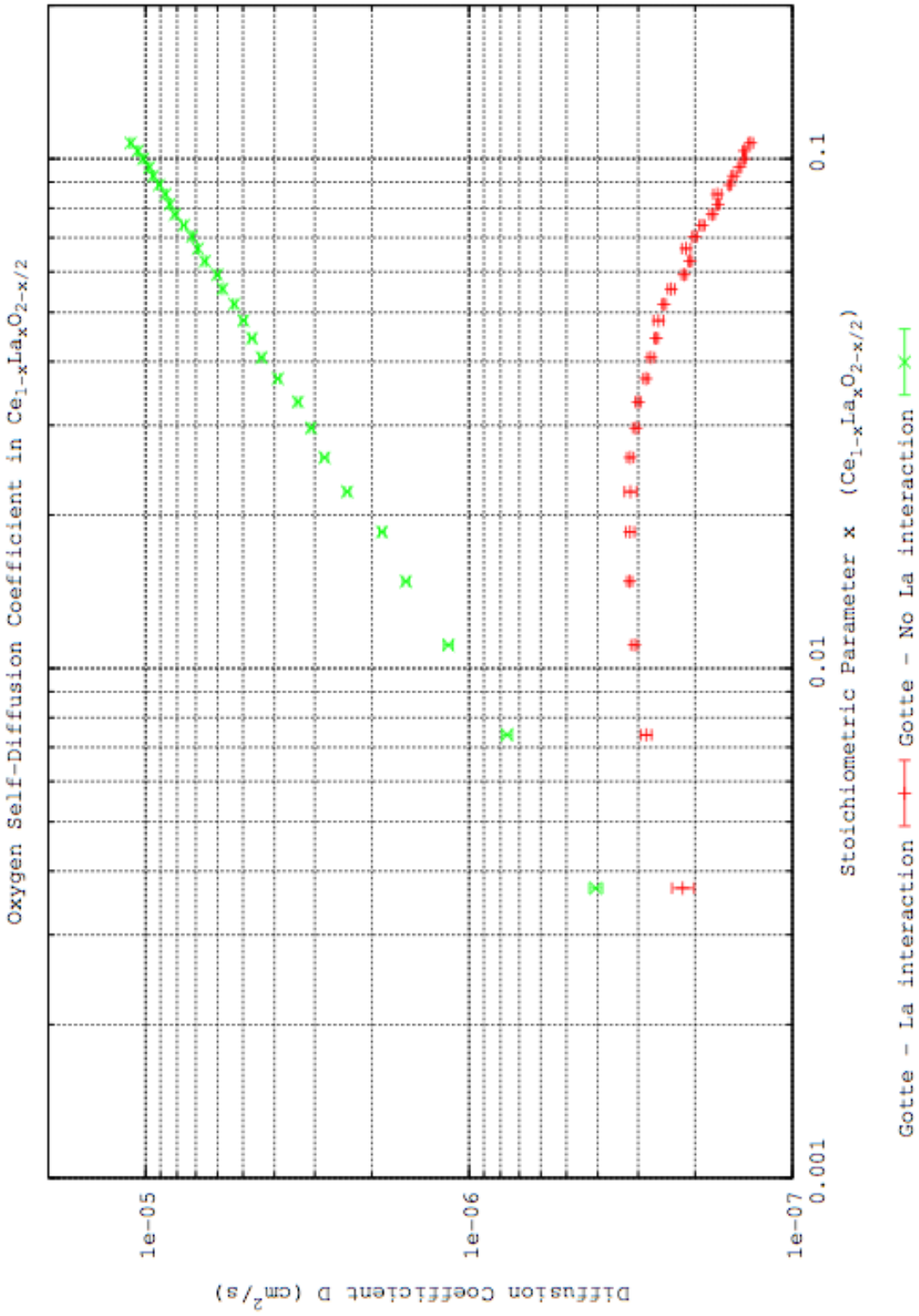

Figure 5.26: KMC simulation Results for Diffusivities Derived From the Gotte Potential [25]

not expected. A more complete KMC study should be conducted to include not only oxygen vacancies but also oxygen interstitials, cerium vacancies and interstitials.

CHAPTER 6

CONCLUSION AND FUTURE WORK

1 MeV Kr ion irradiation experiments have been performed on CeO_2 single crystal with 0 %mol La, 5 mol% La_2O_3 and 25 mol% La_2O_3 at 800C. *In-Situ* TEM results show that the evolution of dislocation loop becoming nucleation, growth and interactions during irradiation. The 25 mol% La doped sample had the highest growth rate and the 5% La sample had the lowest while pure CeO_2 was in between. The growth rate of dislocation loops is inversely correlated to oxygen vacancy diffusivity. The loop planes accommodating dislocation loops were characterized to be {111} but not {200} or {220}.

The future work will be divided into two parts: microscopy and computing simulations. Since convincing evidence of the structure of dislocation loops in CeO_2 are still lacking, efforts to resolve the structure on the atomic scale are necessary. In addition to the inside-outside contrast technique, high resolution transmission electron microscopy (HRTEM) might be able to determine whether the loops are of interstitial type or vacancy type. If the resolving power is high enough, the nature of the dislocation loops (one layer or three layers of interstitials) can be determined.

A more sophisticated simulation on the evolutions of dislocation loops in CeO_2 is planned. In addition to oxygen vacancies, the diffusion of oxygen interstitials, cerium vacancies and interstitials should also be considered. The goal will be focused on finding the major factor that control the growing process of the dislocation loops. In addition, it is important to use computer simulation to study the effect of La, and extend the study to other impurities.

APPENDIX A

MORE MICROGRAPHS

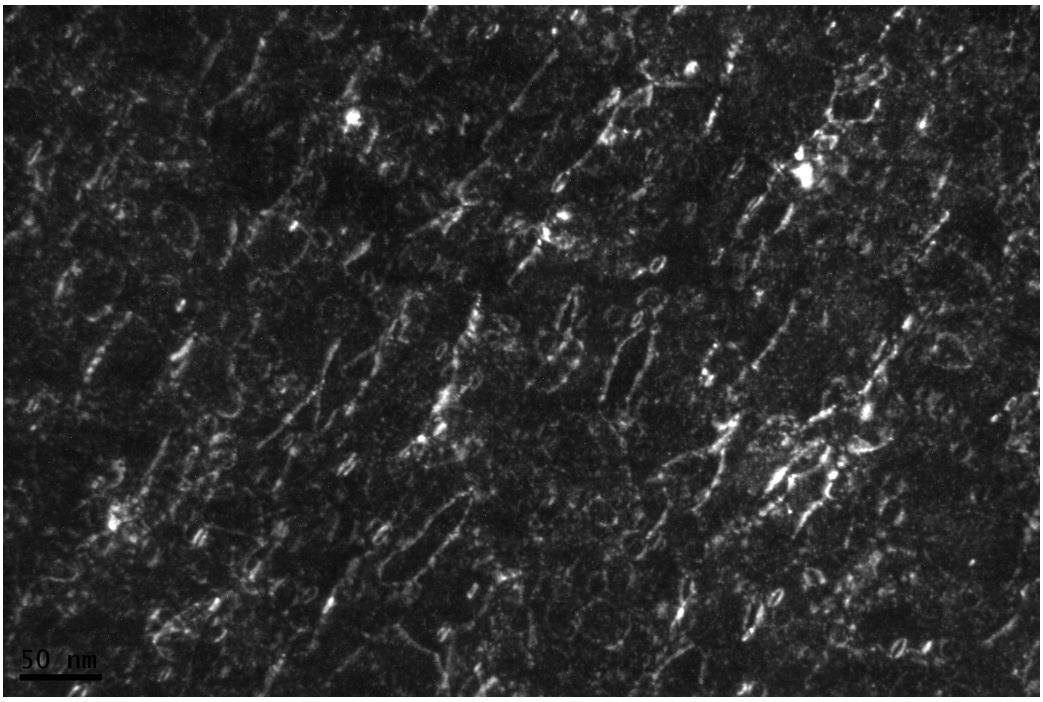

(a) Dark field

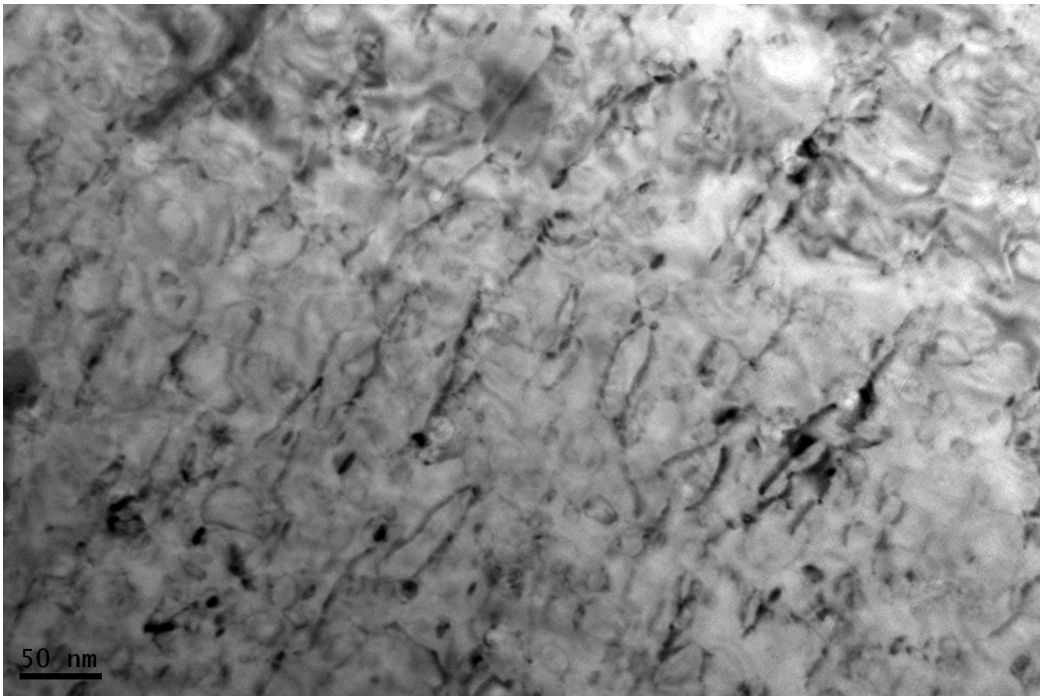

(b) Bright field

Figure A.1: (a)Bright field image and (b) bright field image for 5 mol% La doped CeO_2 at the dose of 1.5 $\times 10^{15}$ ions/cm2. g = (200) at [001] direction

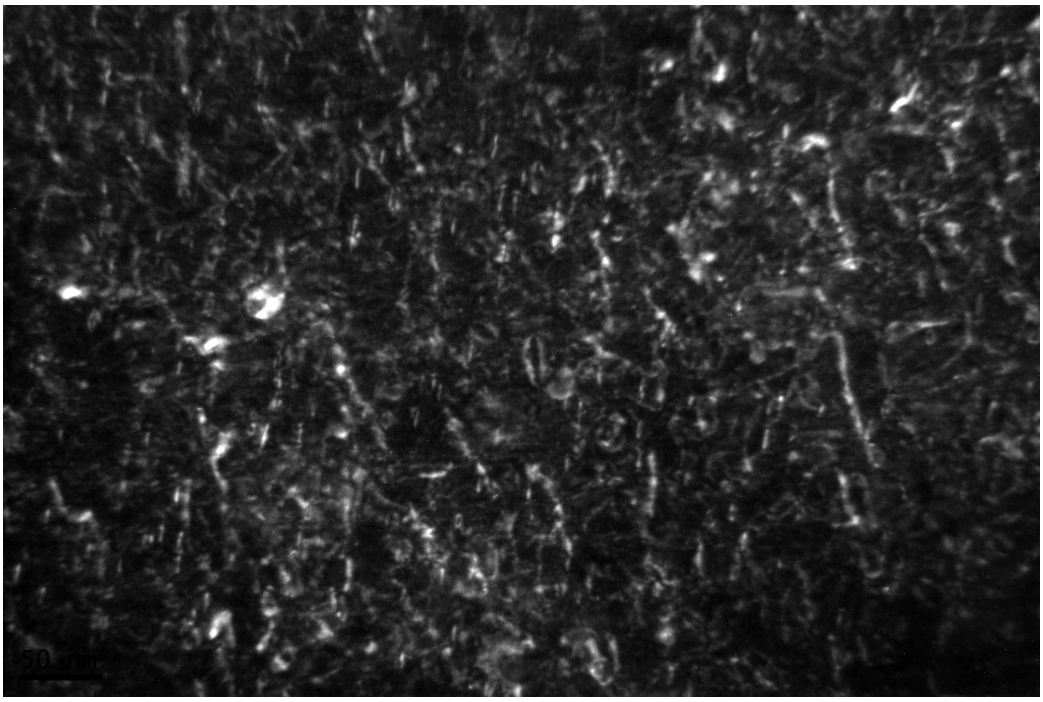

(a) Dark field

(b) Bright field

Figure A.2: (a)Bright field image and (b) bright field image for 5 mol% La doped CeO_2 at the dose of 1.5 $\times 10^{15}$ ions/cm2. g = (110) at $[11\bar{2}]$ direction

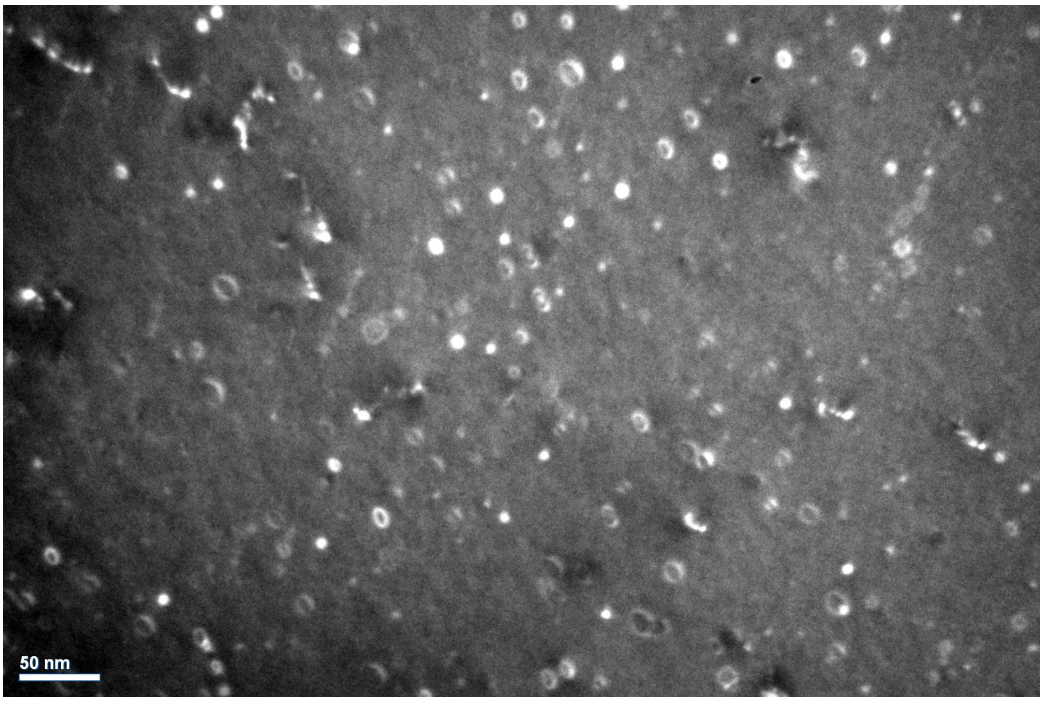

(a) Dark field

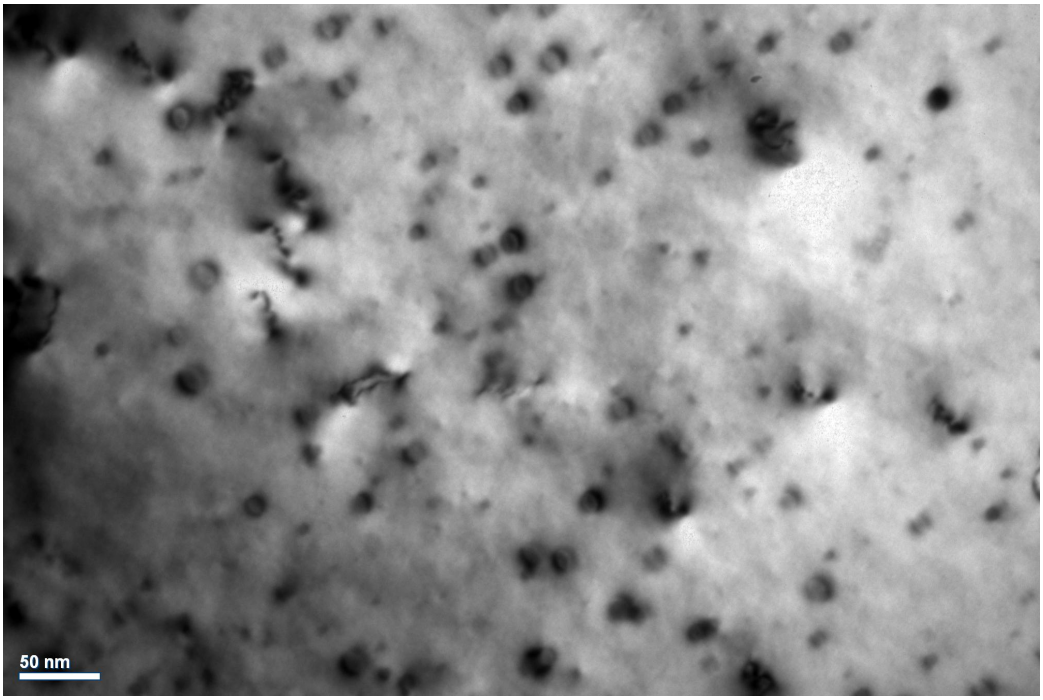

(b) Bright field

Figure A.3: (a)Bright field image and (b) bright field image for 25 mol% La doped CeO_2 at the dose of 1 $\times 10^{14}$ ions/cm2. g = (220) at [100] direction

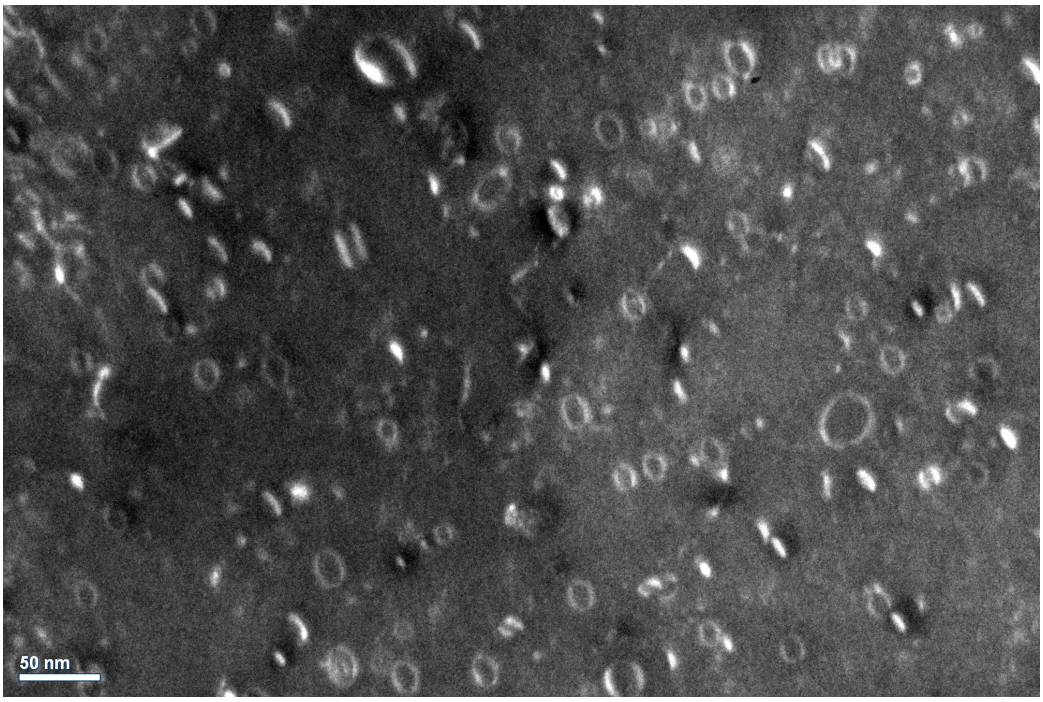

(a) Dark field

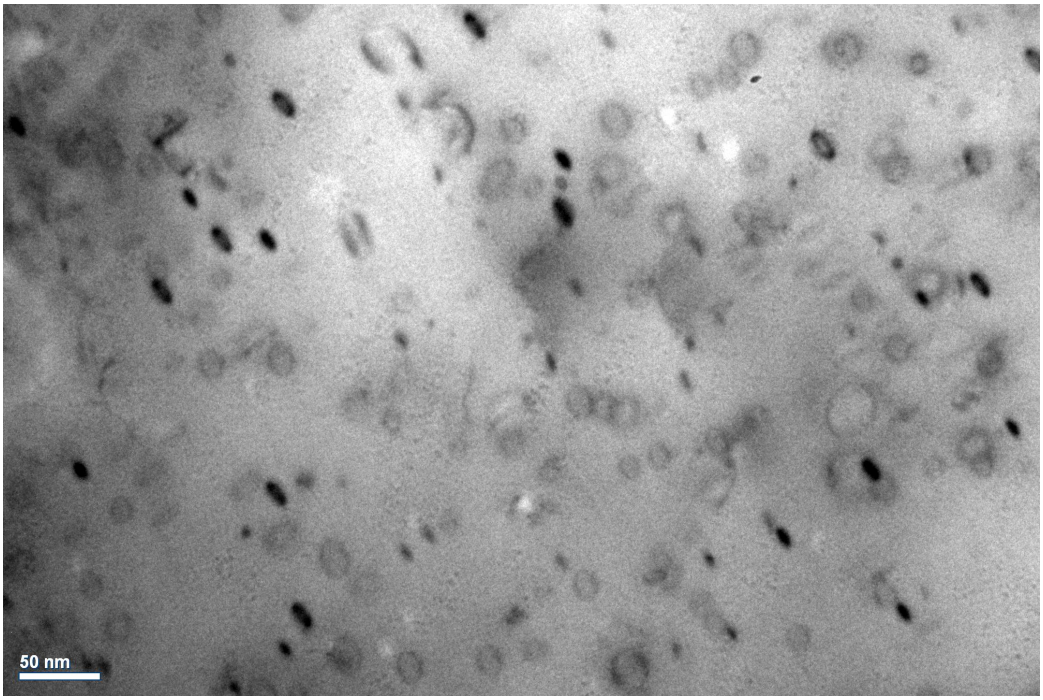

(b) Bright field

Figure A.4: (a)Bright field image and (b) bright field image for 25 mol% La doped CeO_2 at the dose of 3 $\times 10^{14}$ ions/cm2. g = (220) at [100] direction

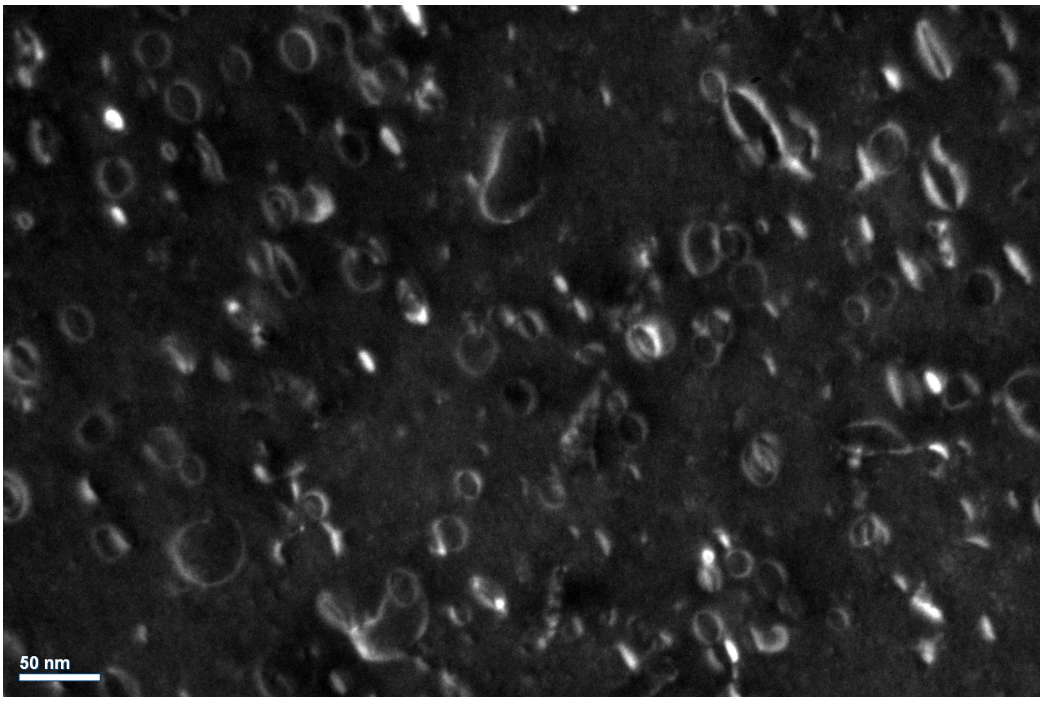

(a) Dark field

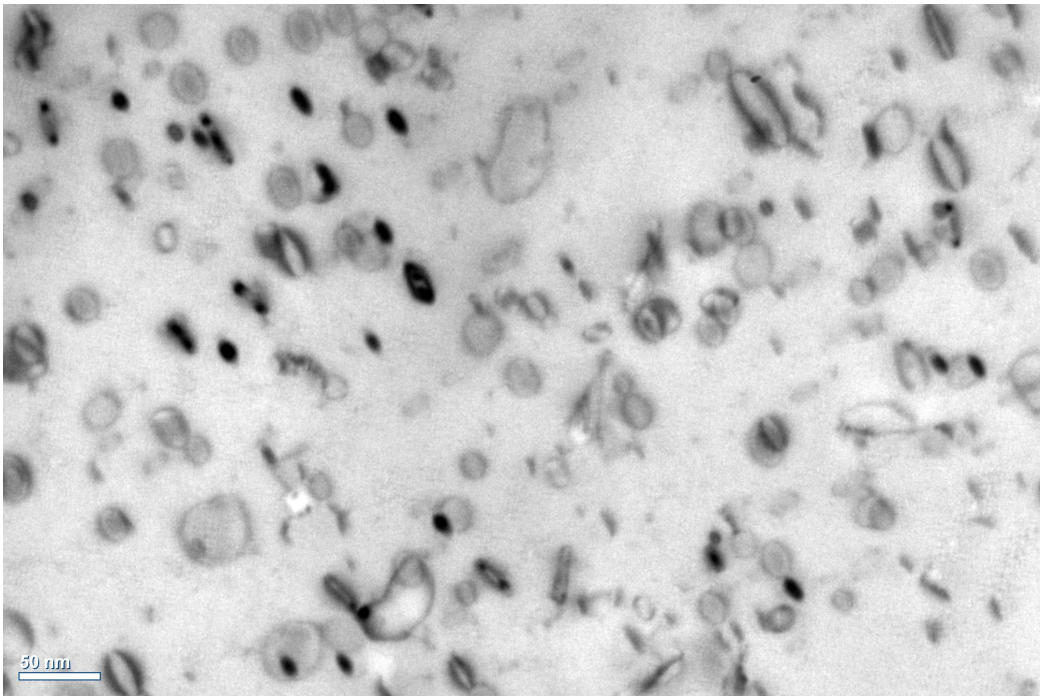

(b) Bright field

Figure A.5: (a)Bright field image and (b) bright field image for 25 mol% La doped CeO_2 at the dose of 5 $\times 10^{14}$ ions/cm2. g = (220) at [100] direction

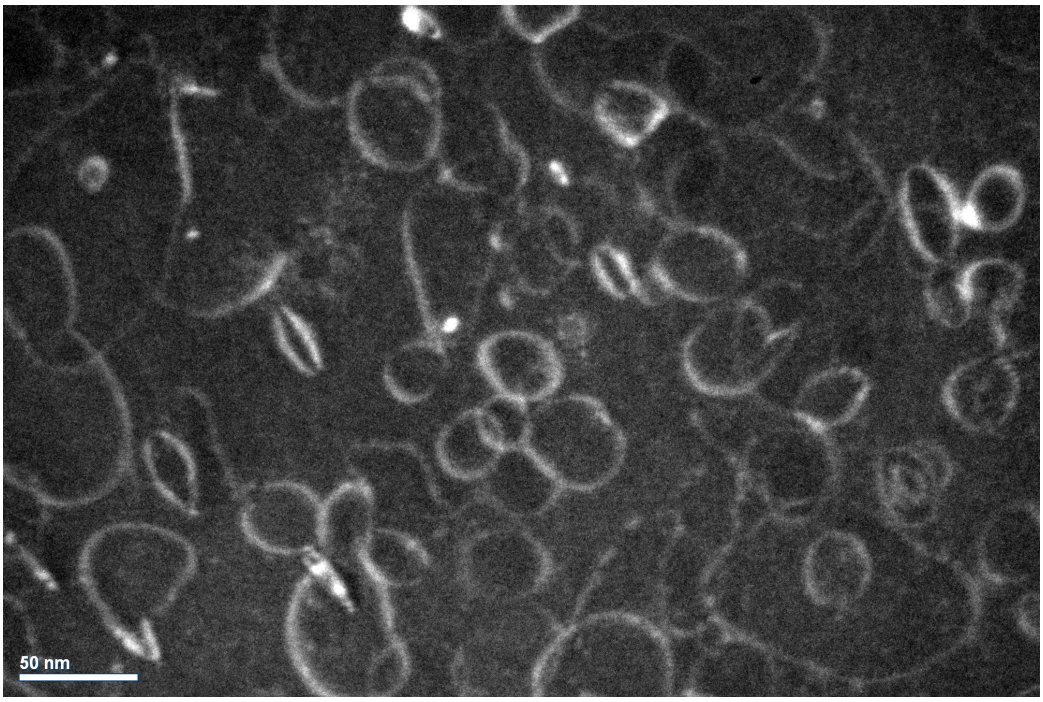

(a) Dark field

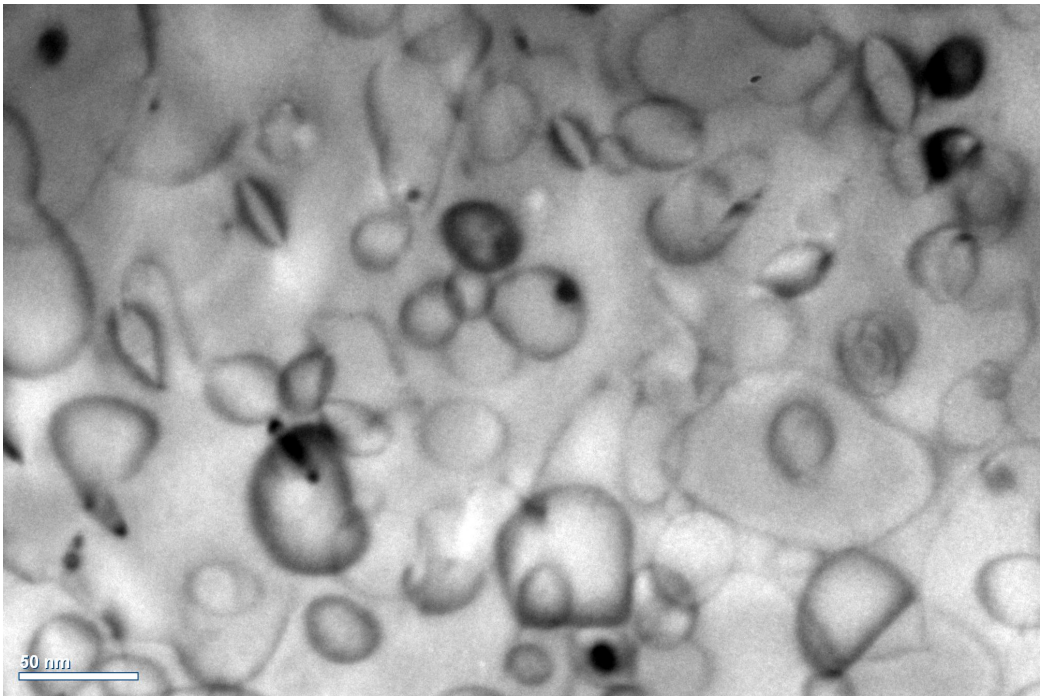

(b) Bright field

Figure A.6: (a)Bright field image and (b) bright field image for 25 mol% La doped CeO_2 at the dose of 8 $\times 10^{14}$ ions/cm2. g = (220) at [100] direction

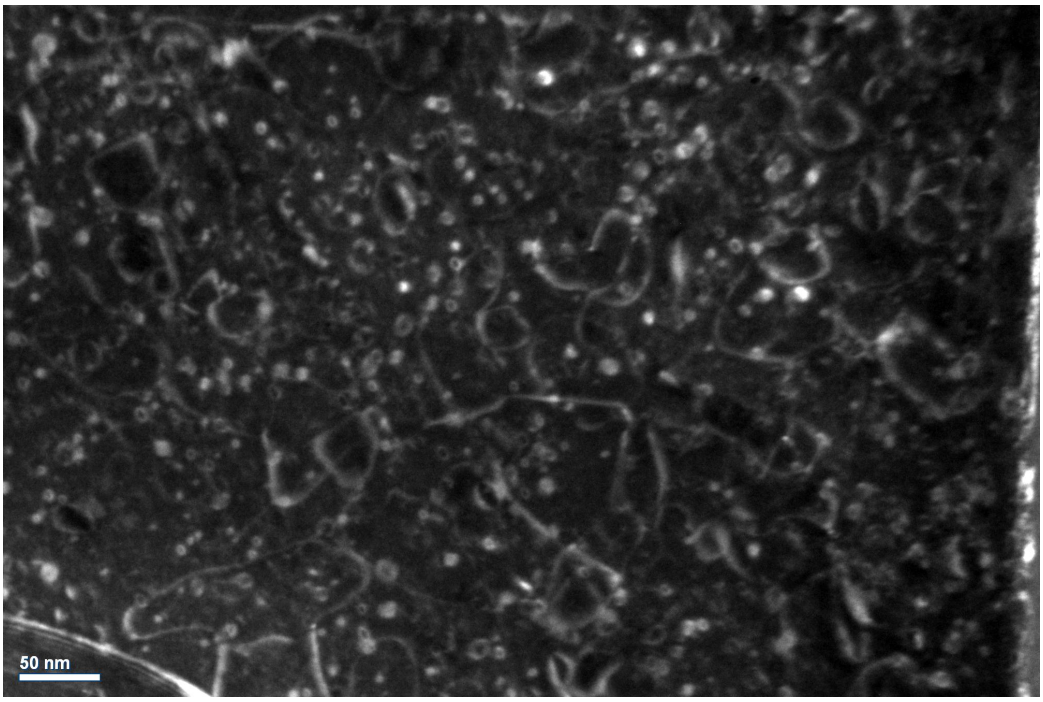

(a) Dark field

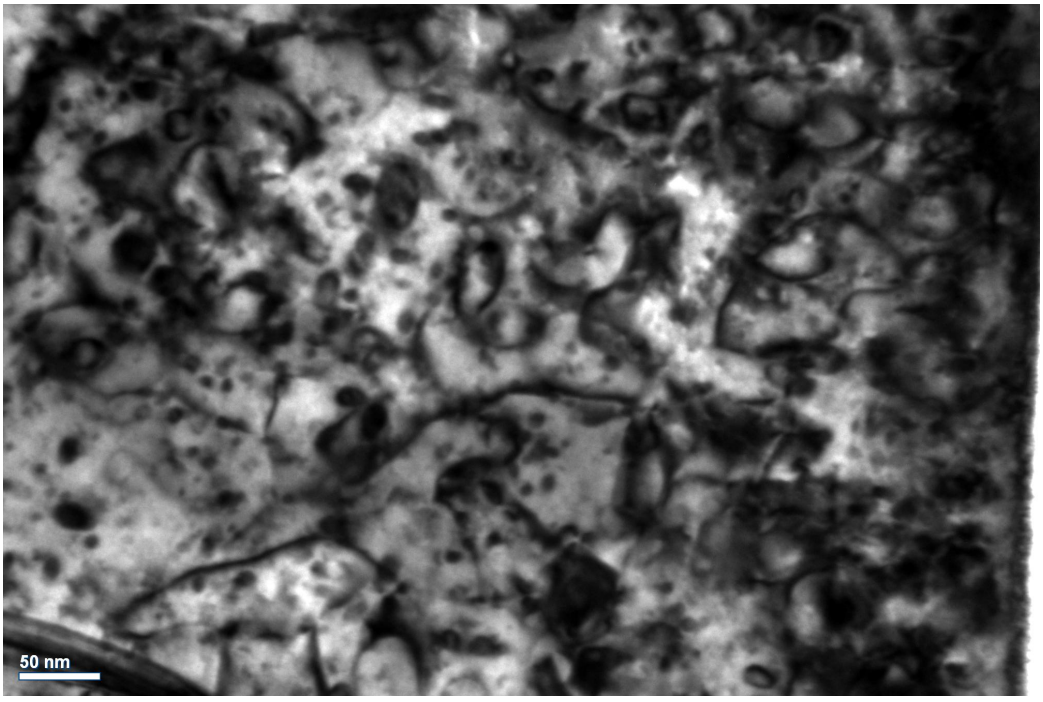

(b) Bright field

Figure A.7: (a)Bright field image and (b) bright field image for 25 mol% La doped CeO_2 at the dose of 1.5 $\times 10^{15}$ ions/cm2. g = (220) at [100] direction

REFERENCES

[1] G. Lucas, "The evolution of mechanical property change in irradiated austenitic stainless steels," *Journal of Nuclear Materials*, vol. 206, no. 2-3, pp. 287–305, Nov. 1993. [Online]. Available: http://www.sciencedirect.com/science/article/B6TXN-47YRS4C-7H/2/d3438c79fdcad4cc8bed18044567c7f4

[2] P. Scott, "A review of irradiation assisted stress-corrosion cracking," *Journal of Nuclear Materials*, vol. 211, no. 2, pp. 101–122, Aug. 1994.

[3] B. M. Institute, *Refractory ceramics for aerospace: a materials selection handbook*, J. R. H. [and others], Ed. American Ceramic Society, Columbus, Ohio, 1964.

[4] K. Yasunaga, K. Yasuda, S. Matsumura, and T. Sonoda, "Nucleation and growth of defect clusters in ceo2 irradiated with electrons," *Nuclear Instruments and Methods in Physics Research Section B: Beam Interactions with Materials and Atoms*, vol. 250, no. 1-2, pp. 114–118, Sep. 2006. [Online]. Available: http://www.sciencedirect.com/science/article/B6TJN-4K7NHDH-4/2/0cd87d0a8dbfe830f66de8305f77d0fd

[5] K. Yasunaga, K. Yasuda, S. Matsumura, and T. Sonoda, "Electron energy-dependent formation of dislocation loops in ceo2," *Nuclear Instruments and Methods in Physics Research Section B: Beam Interactions with Materials and Atoms*, vol. 266, no. 12-13, pp. 2877–2881, June 2008. [Online]. Available: http://www.sciencedirect.com/science/article/B6TJN-4S5VCG2-3/2/f34bac401804bfd23bb2385257614744

[6] T. Sonoda, M. Kinoshita, Y. Chimi, N. Ishikawa, M. Sataka, and A. Iwase, "Electronic excitation effects in ceo2 under irradiations with high-energy ions of typical fission products," *Nuclear Instruments and Methods in Physics Research Section B: Beam Interactions with Materials and Atoms*, vol. 250, no. 1-2, pp. 254–258, Sep. 2006. [Online]. Available: http://www.sciencedirect.com/science/article/B6TJN-4KBX4CC-1/2/0abbbb4925599bc585a63cf39b0eabb2

[7] T. Sonoda, M. Kinoshita, N. Ishikawa, M. Sataka, Y. Chimi, N. Okubo, A. Iwase, and K. Yasunaga, "Clarification of the properties and accumulation effects of ion tracks in ceo2," *Nuclear Instruments and Methods in Physics Research Section B: Beam Interactions with Materials and Atoms*, vol. 266, no. 12-13, pp. 2882–2886, June 2008. [Online]. Available: http://www.sciencedirect.com/science/article/B6TJN-4S62RFV-2/2/ed21d12ca961a20beaf948ad650b37b6

[8] B. Zhu, H. Ohno, S. Kosugi, F. Hori, K. Yasunaga, N. Ishikawa, and A. Iwase, "Effects of swift heavy ion irradiation on the structure of er2o3-doped ceo2," *Nuclear Instruments and Methods in Physics Research Section B: Beam Interactions with Materials and Atoms*, vol. 268, no. 19, pp. 3199–3202, Oct. 2010. [Online]. Available: http://www.sciencedirect.com/science/article/B6TJN-5070DB6-2/2/3737927778e20648bc6e2d2547c1dc4c

[9] Y. Tahara, B. Zhu, S. Kosugi, N. Ishikawa, Y. Okamoto, F. Hori, T. Matsui, and A. Iwase, "Study on effects of swift heavy ion irradiation on the crystal structure in ceo2 doped with gd2o3," *Nuclear Instruments and Methods in Physics Research Section B: Beam Interactions with Materials and Atoms*, vol. In Press, Corrected Proof, pp. –. [Online]. Available: http://www.sciencedirect.com/science/article/B6TJN-51PRY19-H/2/b088a998e86e4695904f2cbb0218fdfd

[10] K. Shiiyama, T. Yamamoto, T. Takahashi, A. Guglielmetti, A. Chartier, K. Yasuda, S. Matsumura, K. Yasunaga, and C. Meis, "Molecular dynamics simulations of oxygen frenkel pairs in cerium dioxide," *Nuclear Instruments and Methods in Physics Research Section B: Beam Interactions with Materials and Atoms*, vol. 268, no. 19, pp. 2980–2983, Oct. 2010. [Online]. Available: http://www.sciencedirect.com/science/article/B6TJN-5023KD6-9/2/fef2413c200fd3ec2a90ce6b00654829

[11] B. Ye, D. Yun, A. Oaks, W. Chen, M. Kirk, J. Rest, A. Yacout, and J. Stubbins, "The effects of xenon implantation in ceria with and without lanthanum," *Nuclear Instruments and Methods in Physics Research Section B: Beam Interactions with Materials and Atoms*, vol. In Press, Corrected Proof, pp. –, 2011. [Online]. Available: http://www.sciencedirect.com/science/article/B6TJN-5236R3X-1D/2/e4354c895c6c54d31cde6c624d98b793

[12] D. Yun, B. Ye, A. Oaks, W. Chen, M. Kirk, J. Rest, A. Yacout, and J. Stubbins, "Fission gas transport and its interactions with irradiation-induced defects in lanthanum doped ceria," *Nuclear Instruments and Methods in Physics Research Section B: Beam Interactions with*

Materials and Atoms, vol. In Press, Corrected Proof, pp. –, 2011. [Online]. Available: http://www.sciencedirect.com/science/article/B6TJN-5236R3X-1F/2/2c7a7eb30c0ecc1ac20d67da9aacb368

[13] D. S. Aidhy, P. C. Millett, T. Desai, D. Wolf, and S. R. Phillpot, "Kinetically evolving irradiation-induced point defect clusters in uo2 by molecular dynamics simulations," *Phys. Rev. B*, vol. 80, no. 10, pp. 104 107–, Sep. 2009. [Online]. Available: http://link.aps.org/doi/10.1103/PhysRevB.80.104107

[14] J. Jonnet, "A contribution to the understanding of the high burn-up structure formation in nuclear fuels," Ph.D. dissertation, National Polytechnic Institute of Lorraine, 2007.

[15] e. a. J.F. Ziegler, J.P. Biersack, *The Stopping and Range of Ions of Solids*. Pergamon Press, New York, 1985.

[16] A. Trovarelli, *Catalysis By Ceria and Related Materials, ser. Catalytic Science Series*. Imperial College Press, London, UK, 2002.

[17] R. J. M. Konings, K. Bakker, J. G. Boshoven, R. Conrad, and H. Hein, "The influence of neutron irradiation on the microstructure of al2o3, mgal2o4, y3al5o12 and ceo2," *Journal of Nuclear Materials*, vol. 254, no. 2-3, pp. 135 – 142, 1998. [Online]. Available: http://www.sciencedirect.com/science/article/B6TXN-3V6X3W7-4/2/194d51d31b81284b485631a60fdea00c

[18] L. Minervini, M. O. Zacate, and R. W. Grimes, "Defect cluster formation in m2o3-doped ceo2," *Solid State Ionics*, vol. 116, no. 3-4, pp. 339–349, Jan. 1999. [Online]. Available: http://www.sciencedirect.com/science/article/B6TY4-3W1R610-K/2/1fd81cd0adc249c6efadbedc4a915cf4

[19] J. Faber, C. Geoffroy, A. Roux, A. Sylvestre, and AbelardP., "A systematic investigation of the dc electrical conductivity of rare-earth doped ceria," *Applied Physics A Materials Science & Processing*, vol. 49, p. 225.

[20] H. Inaba and H. Tagawa, "Ceria-based solid electrolytes," *Solid State Ionics*, vol. 83, no. 1-2, pp. 1 – 16, 1996. [Online]. Available: http://www.sciencedirect.com/science/article/B6TY4-43PRC8R-1D/2/2651b61f6c96a8412f0d1609f768432e

[21] D. Y. Wang, D. Park, J. Griffith, and A. Nowick, "Oxygen-ion conductivity and defect interactions in yttria-doped ceria," *Solid State Ionics*, vol. 2, no. 2, pp. 95 – 105, 1981. [Online]. Available: http://www.sciencedirect.com/science/article/B6TY4-46J6216-11/2/303b48f6237ced18eec4cbf55c50e307

[22] D. Yun, "Fission gas transport and its interactions with irradiation-induced defects in lanthanum doped ceria," Ph.D. dissertation, University of Illinois at Champaign-Urbana, 2010.

[23] D. B. Williams and C. B. Carter, *Transmission Electron Microscopy-A Textbook for Materials Science*. Springer, 2004.

[24] B. G. Dick and A. W. Overhauser, "Theory of the dielectric constants of alkali halide crystals," *Phys. Rev.*, vol. 112, no. 1, p. 90, Oct 1958.

[25] A. Oaks, D. Yun, B. Ye, W. Chen, and J. F. Stubbins, "Kinetic monte carlo model of defect transport and irradiation effects in la-doped ceo2," *Journal of Nuclear Materials*, vol. In Press, Accepted Manuscript, pp. –, 2011. [Online]. Available: http://www.sciencedirect.com/science/article/B6TXN-526DWW2-5/2/0a9b02387555a94a3dea40d8d3efa929

[26] A. Gotte, D. Spangberg, K. Hermansson, and M. Baudin, "Molecular dynamics study of oxygen self-diffusion in reduced ceo2," *Solid State Ionics*, vol. 178, no. 25-26, pp. 1421–1427, Oct. 2007. [Online]. Available: http://www.sciencedirect.com/science/article/B6TY4-4PSJSJM-1/2/f543728b434a9fef794930ba80819803

[27] J. R. McBride, K. C. Hass, B. D. Poindexter, and W. H. Weber, "Raman and x-ray studies of ce, +rexoz+ where re=la, pr, nci, eu, gd, and .tb," *J. Appl. Phys.*, vol. 76, p. 2435, 1994.

[28] Y. Miao, "Private communication."

[29] D. S. Aidhy, "Private communication."

[30] M. Hayns, "The nucleation and early growth of interstitial dislocation loops in irradiated materials," *Journal of Nuclear Materials*, vol. 56, no. 3, pp. 267–274, June 1975. [Online]. Available: http://www.sciencedirect.com/science/article/B6TXN-47Y9JFT-42/2/b52421727bc67d2a1dd0706b22beee10

[31] J. Gale and A. Rohl, "The general lattice utility program (gulp)," *Mol. Simul.*, vol. 29, p. 291, 2003.

[32] S. Plimpton, "Fast parallel algorithms for short-range molecular dynamics," *J Comp Phys*, vol. 117, pp. 1–19, 1995.

AUTHOR'S BIOGRAPHY

Weiying Chen received his B.S. in Engineering and System Science from National Tsing Hua University, Taiwan in July 2005. After that he worked as a research assistant in the same department. The education in college and experience at work inspired him to pursue further study in field of nuclear engineering and science. He became a graduate student of Department of Nuclear, Plasma and Radiology Engineering at University of Illinois at Urbana-Champaign in August 2008. He will continue his studies in the field of nuclear engineering through his Ph.D.